Featured in Physics

Amplitude analysis of $B^0 \to \overline{D}^0 D_s^+ \pi^-$ and $B^+ \to D^- D_s^+ \pi^+$ decays

R. Aaij *et al.*[*]

(LHCb Collaboration)

Resonant contributions in $B^0 \to \bar{D}^0 D_s^+ \pi^-$ and $B^+ \to D^- D_s^+ \pi^+$ decays are determined with an amplitude analysis, which is performed both separately and simultaneously, where in the latter case isospin symmetry between the decays is assumed. The analysis is based on data collected by the LHCb detector in proton-proton collisions at center-of-mass energies of 7, 8, and 13 TeV. The full data sample corresponds to an integrated luminosity of 9 fb^{-1}. A doubly charged spin-0 open-charm tetraquark candidate together with a neutral partner, both with masses near 2.9 GeV, are observed in the $D_s \pi$ decay channel.

I. INTRODUCTION

The decays of b hadrons into final states involving two open-charm hadrons form a large family of topologically similar processes that include many intermediate states such as charmonia, highly excited $D_{(s)}$ states, and possible exotic hadrons. The Dalitz plot distributions of $B^0 \to D^0 D^- K^+$, $B^+ \to D^0 \overline{D}^0 K^+$, and $B^+ \to D^+ D^- K^+$ decays[1] have already been explored by the Belle [1], *BABAR* [2], and LHCb collaborations [3,4]. In these studies, the discovery of the charm-strange meson $D_{s1}(2700)^+$, the charmoniumlike state $\chi_{c0}(3930)$, and the open-charm tetraquark state $X_{0,1}(2900)$ were reported, prompting many theoretical investigations into the internal structure of these states [5].

The decays $B^+ \to D^- D_s^+ \pi^+$ and $B^0 \to \overline{D}^0 D_s^+ \pi^-$ are yet to be explored. They are ideal to study excited D mesons (D^{**}) with natural spin-parity, to test isospin symmetry in the charged and neutral $D\pi$ resonances, and to test QCD predictions [6]. The $D^*(2007)^0$, $D^*(2010)^+$, $D_0^*(2300)$, and $D_2^*(2460)$ mesons are already well established. The $D_1^*(2600)^0$ and $D_J^*(3000)^0$ mesons were recently discovered in the inclusive proton-proton (pp) collisions and in B decays [7], while their charged isospin partners have not been observed, although some measurements suggest their existence [8]. These states could also be explored in $B \to \bar{D}D_s^+ \pi$ decays. Figure 1 shows the Feynman diagrams

[*]Full author list given at the end of the article.
[1]Charge conjugation is implied throughout this paper.

of the dominant tree-level amplitudes contributing to the two decays.

Studies of $B \to \bar{D}D_s^+ \pi$ decays also provide an excellent opportunity to search for exotic hadrons decaying into the $D_s^+ \pi$ and $\bar{D}D_s^+$ final states. The discoveries of the $D_{s0}^*(2317)^+$ [9] and $D_{s1}(2460)^+$ [10] states prompted speculation that they may have a tetraquark component [6,7]. No evidence for isospin partners has been found in explicit searches [11,12], but if they exist they should contribute to the $B \to \bar{D}D_s^+ \pi$ decays. The D0 collaboration claimed evidence for an $X(5568)$ state [13,14], which however was not confirmed by other experiments [15–18]. An open-charm tetraquark state with four different quark flavors, analogous to the $X(5568)$ state, is predicted by the diquark-antidiquark model [19,20], and can be investigated in $D_s^+ \pi^\pm$ final states. In particular, the $D_s^+ \pi^+$ channel presents an attractive potential according to lattice QCD calculation [21], which can form a tetraquark resonance. Some theoretical studies on the $X_{0,1}(2900)$ state suggest searching for a potential doubly charged charm-strange tetraquark candidate, together with its neutral isospin partner, in the $D_s^+ \pi^+ [c\bar{s}u\bar{d}]$ and $D_s^+ \pi^- [c\bar{s}\,\bar{u}\,d]$ final states [22–27]. In addition, searches for possible $\bar{D}D_s^+$ resonances are well motivated by the recent observations of the open-strange hidden-charm tetraquark state $Z_{cs}(3985)$ decaying into $\bar{D}^* D_s^+ + \bar{D}D_s^{*+}$ at BESIII [28,29], as well as the $Z_{cs}(4000)$ and $Z_{cs}(4220)$ states decaying into KJ/ψ at LHCb [30].

In this paper, an amplitude analysis of $B^+ \to D^- D_s^+ \pi^+$ and $B^0 \to \overline{D}^0 D_s^+ \pi^-$ decays is presented for the first time, revealing the contributions of $\bar{D}\pi$ resonances in the two decays, and allowing searches for possible exotic states. As the two channels are closely related by isospin, three different fit scenarios are performed: a fit performed independently on the two decay channels is called the

(a)

(b)

(c)

(d)
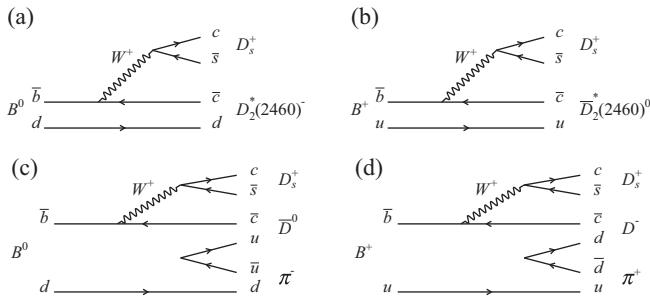
FIG. 1. Feynman diagrams for the dominant tree-level amplitudes contributing to (a) $B^0 \to \overline{D}^0 D_s^+ \pi^-$ and (b) $B^+ \to D^- D_s^+ \pi^+$ decays with intermediate $D\pi$ resonances; and nonresonant three body decays of (c) $B^0 \to \overline{D}^0 D_s^+ \pi^-$ and (d) $B^+ \to D^- D_s^+ \pi^+$ decays.

separate fit; a simultaneous fit of the $B^0 \to \overline{D}^0 D_s^+ \pi^-$ and $B^+ \to D^- D_s^+ \pi^+$ decays, by assuming that all the $\bar{D}\pi$ resonances in the two decays are isospin related, is denoted the simultaneous $\bar{D}\pi$ fit; a simultaneous fit, in which all the parameters of $\bar{D}\pi$ states and potential $D_s^+ \pi$ or DD_s^+ resonances are shared between the two decays, is called the full simultaneous fit. The separate fit and simultaneous $\bar{D}\pi$ fit are discussed in this paper, while the full simultaneous fit, which is considered as the default result of this analysis, is described in Ref. [31]. The analysis is based on pp collision data collected using the LHCb detector, corresponding to a total integrated luminosity of 3 fb^{-1} at center-of-mass energies $\sqrt{s} = 7, 8$ TeV, referred to as run 1, and 6 fb^{-1} at $\sqrt{s} = 13$ TeV, referred to as run 2.

The paper is organized as follows. A brief introduction of LHCb detector and reconstruction and simulation procedures is provided in Sec. II. The event selection criteria are shown in Sec. III, and signal and background yields are determined in Sec. IV. The formalism of amplitude analysis is summarized in Sec. V. The signal efficiency and background models in amplitude analysis are studied in Sec. VI. The separate fit result is presented in Sec. VII, while the result from simultaneous $\bar{D}\pi$ fit is provided in Sec. VIII. The systematic uncertainties are evaluated in Sec. IX. All the results are summarized in Sec. X.

II. LHCb DETECTOR AND SIMULATION

The LHCb detector [32,33] is a single-arm forward spectrometer covering the pseudorapidity range $2 < \eta < 5$, designed for the study of particles containing b or c quarks. The detector includes a high-precision tracking system consisting of a silicon-strip vertex detector surrounding the pp interaction region, a large-area silicon-strip detector located upstream of a dipole magnet with a bending power of about 4 Tm, and three stations of silicon-strip detectors and straw drift tubes placed downstream of the magnet. The tracking system provides a measurement of the momentum, p, of charged particles with a relative uncertainty that varies

from 0.5% at low momentum to 1.0% at 200 GeV.[2] The minimum distance of a track to a primary pp collision vertex (PV), the impact parameter (IP), is measured with a resolution of $(15 + 29/p_T)$ μm, where p_T is the component of the momentum transverse to the beam, in GeV. Different types of charged hadrons are distinguished using information from two ring-imaging Cherenkov detectors. Photons, electrons, and hadrons are identified by a calorimeter system consisting of scintillating-pad and pre-shower detectors, an electromagnetic and a hadronic calorimeter. Muons are identified by a system composed of alternating layers of iron and multiwire proportional chambers. The online event selection is performed by a trigger, which consists of a hardware stage, based on information from the calorimeter and muon systems, followed by a software stage, which applies a full event reconstruction.

At the hardware trigger stage, events are required to have a muon with high p_T or a hadron, photon, or electron with high transverse energy in the calorimeters. For hadrons, the transverse energy threshold is 3.5 GeV. The software trigger requires a two-, three-, or four-track secondary vertex with a significant displacement from any primary pp interaction vertex. At least one charged particle must have a transverse momentum $p_T > 1.6$ GeV and be inconsistent with originating from a PV. A multivariate algorithm [34,35] is used for the identification of secondary vertices consistent with a decay of a b hadron.

Simulation is used to model the effects of the detector acceptance and the imposed selection requirements. In the simulation, pp collisions are generated using PYTHIA 8 [36,37] with a specific LHCb configuration [38]. Decays of unstable particles are described by EvtGen [39], in which final-state radiation is generated using PHOTOS [40]. The interaction of the generated particles with the detector, and its response, are implemented using the Geant4 toolkit [41,42] as described in Ref. [43]. The underlying pp interaction is reused multiple times, with an independently generated signal decay for each [44].

The particle identification (PID) response for charged tracks in the simulated samples is corrected based on special samples of $D^{*+} \to D^0 \pi^+$, $D^0 \to K^- \pi^+$ decays. For each PID response of a track, the unbinned four-dimensional probability density functions (PDFs) for the data, $p_{\text{data}}(x|p_T, \eta, N_{\text{tr}})$, and for the simulated samples $p_{\text{sim}}(x|p_T, \eta, N_{\text{tr}})$ are extracted based on a kernel density estimation [45], where x is the PID response, p_T and η are the transverse momentum and pseudorapidity of the track, and N_{tr} is the number of tracks in the event. The cumulative distribution functions for the data $P_{\text{data}}(x|p_T, \eta, N_{\text{tr}})$ and for the simulated samples $P_{\text{sim}}(x|p_T, \eta, N_{\text{tr}})$ are determined, and the corrected PID response in the simulated samples is evaluated by transforming the x_{sim} into x_{corr} with

---

[2]Natural units with $\hbar = c = 1$ are used throughout this paper.

$$x_{\text{corr}} = P_{\text{data}}^{-1}(P_{\text{sim}}(x_{\text{sim}}|p_{\text{T}}, \eta, N_{\text{tr}})|p_{\text{T}}, \eta, N_{\text{tr}}). \quad (1)$$

During the transformation, the N_{tr} distribution in the simulated samples is scaled by a factor to match the same distribution in the corresponding datasets. The PID response in the simulated samples shows good agreement with that in the data samples after the correction.

The momentum scale is calibrated using control samples of $J/\psi \to \mu^+\mu^-$ and $B^+ \to J/\psi K^+$ decays collected concurrently with the data samples used for this analysis [46,47]. The relative uncertainty on the momentum scale is 3×10^{-4}.

III. SELECTION

In LHCb, trigger decisions are associated with reconstructed particles. Selection requirements can therefore be made on the trigger selection itself and on whether the decision was due to the signal candidate, other particles produced in the pp collision, or a combination of both.

In the analysis, the $B^0 \to \bar{D}^0 D_s^+ \pi^-$ and $B^+ \to D^- D_s^+ \pi^+$ candidates are formed using charged kaon and pion candidates, in which the $\bar{D}^0$ candidates is reconstructed through the $\bar{D}^0 \to K^+\pi^-$ and $\bar{D}^0 \to K^+\pi^-\pi^-\pi^+$ decays, D^+ through the $D^+ \to K^-\pi^+\pi^+$ decays, and D_s^+ through the $D_s^+ \to K^+K^-\pi^+$ decays. The invariant mass of $\bar{D}^0\pi^-$ is required to be larger than 2.05 GeV in order to veto the contribution from the $B^0 \to D^{*-}D_s^+$ decay, which is not the focus of this analysis. To consider potential variations of signal efficiencies and background distributions, selections are designed and optimized separately for the six datasets, namely run 1 and run 2 datasets with three reconstruction channels, $B^0 \to \bar{D}^0_{K^+\pi^-}D_s^+\pi^-$, $B^0 \to \bar{D}^0_{K^+\pi^-\pi^-\pi^+}D_s^+\pi^-$, and $B^+ \to D^-D_s^+\pi^+$ decay.

Loose requirements on the p, p_{T}, PID response, and minimum χ^2_{IP} of the charged tracks are first applied to improve track quality and remove tracks originating directly from the pp collision. Here χ^2_{IP} is defined as the difference in the vertex-fit χ^2 of a given PV reconstructed with and without the considered track. To separate B and $D_{(s)}$ candidates from random combinations of tracks directly produced in pp collisions, loose requirements on the invariant mass and on the χ^2 of the flight distance of D candidates with respect to the associated PV are imposed, where the associated PV is defined as the PV yielding the smallest χ^2_{IP} for the considered B candidate. The quantity $\cos\theta_{\text{dir}}$ for a B candidate, where θ_{dir} is the angle between the momentum direction and the vector from the associated PV to the vertex of the candidate, is required to be close to unity.

A boosted decision tree (BDT) classifier [48,49] implemented in the TMVA toolkit [50,51] is used to further suppress the combinatorial background. The BDT classifier depends on the χ^2_{IP} of the B, D, D_s candidates and the final

tracks, the χ^2 of the B decay vertex and its $\cos\theta_{\text{dir}}$, the PID response of all the final tracks, and the signed significance of the separation of $D_{(s)}$ and B vertices parallel to the beam pipe ($s_{z-\text{FD}}^{D_{(s)}}$). For the BDT classifier training, the signal samples are the simulated signal candidates, and the backgrounds are B sideband candidates in data with B invariant mass within $[5500, 6950]$ MeV. The requirement on the BDT response is determined by maximizing $S^2/(S+B)^{\frac{3}{2}}$, where the S and B are the expected signal and background yields in the signal mass window $|M(B) - m(B)| < 20$ MeV, which is 2.5 to 3 times wider than the mass resolution for the different channels, where the $M(B)$ and $m(B)$ are the reconstructed and known masses of the corresponding B meson [7], respectively.

Two kinds of misidentified backgrounds are vetoed through additional requirements. A background to the $B^+ \to D^- D_s^+ \pi^+$ signal occurs at the mass threshold of the $D_s^+\pi^+$ spectrum due to $e^+ - \pi^+$ misidentification. It is removed by a stringent requirement on the PID response of the companion pion. For $B^0 \to \bar{D}^0 D_s^+ \pi^-$, $B_s^0 \to \bar{D}^0 D_s^+ K^-$, and $\bar{\Lambda}_b^0 \to \bar{D}^0 D_s^+ \bar{p}$ decays, misidentified candidates are vetoed by tightening PID requirements of the companion π^- for candidates with invariant mass within ± 30 MeV of the B_s^0 or $\bar{\Lambda}_b^0$ mass [7], after replacing the mass hypothesis of the companion π^- to K^- or $\bar{p}$.

A track-swapped background is found to peak in the B signal region where the π^- from D^{*-} in the $B^0 \to D^{*-}D_s^+$, $D^{*-} \to \bar{D}^0 \pi^-$, $\bar{D}^0 \to K^+\pi^-\pi^-\pi^+$ candidates is swapped with a π^- in the $\bar{D}^0$ decays. As the momentum of the π^- in D^{*-} decays is almost zero in the D^{*-} rest frame, this type of background is removed by requiring $M(K^+\pi^-\pi^-\pi^+) - M(K^+\pi^-\pi^+) > 160$ MeV in the $\bar{D}^0$ decays, to veto those π^- with negligible momentum.

Backgrounds with the same final-state tracks but with one or even zero intermediate charmed mesons, called non-double-charm backgrounds, are suppressed by the requirements on $s_{z-\text{FD}}^{D_{(s)}}$. After the selection, the invariant mass distributions of all possible two-body and three-body combinations of the final charged tracks in $D_{(s)}$ sideband samples are further checked, and all the visible narrow structures, namely $K^*(892)^0$, ϕ, D^0, D^+, and D_s^+ particles, are vetoed to further suppress the non-double-charm backgrounds.

After applying the full off-line selection, the D and D_s masses are required to lie within ± 15 MeV around their known mass [7], corresponding to two to three times the detector resolution. Roughly 1% to 2% of events contain more than one B candidate; one is retained at random in these cases.

To improve the resolution of B candidate invariant mass distributions, a fit based on the Kalman filter method [52], which contains topological and kinematic information of the decay chain, is applied. By updating the four-momentum of all the final-state tracks, the invariant mass of D and D_s

candidates is constrained to the their known masses [7], and the updated invariant mass distributions of B candidates are used to determine the signal and background yields. The four-momenta of charged tracks from another fit, which additionally constrains B candidate mass to the known B mass, are used to calculate kinematic variables used in the amplitude fit.

IV. SIGNAL YIELD DETERMINATION

Figure 2 shows the invariant mass distributions of the B^0 and B^+ candidates in each dataset after the application of the selection requirements. An extended unbinned maximum-likelihood fit to the data in the mass range [5230, 5630] MeV is used to extract the signal and background yields, which are used later in the amplitude fit.

The total PDF comprises a signal PDF and an exponential function to describe the distribution of combinatorial background. The signal PDF is a double-sided crystal ball (DSCB) function [53] which consists of a Gaussian kernel and independent tail parameters on both the left and right sides to model effects such as the detector resolution and final-state radiation. In the fit, the signal and background yields, the parameters of the exponential function, and those of the Gaussian kernel in the DSCB function are allowed to vary independently in each dataset, while the tail parameters are fixed to the values obtained from a fit to the corresponding simulated sample.

In the $\overline{D}^0 D_s^+ \pi^-$ mode, an additional DSCB function is included in the fit model to describe the singly Cabibbo-suppressed $B_s^0 \to \overline{D}^0 D_s^+ \pi^-$ contribution, whose yield is determined from data. The width of the Gaussian kernel is
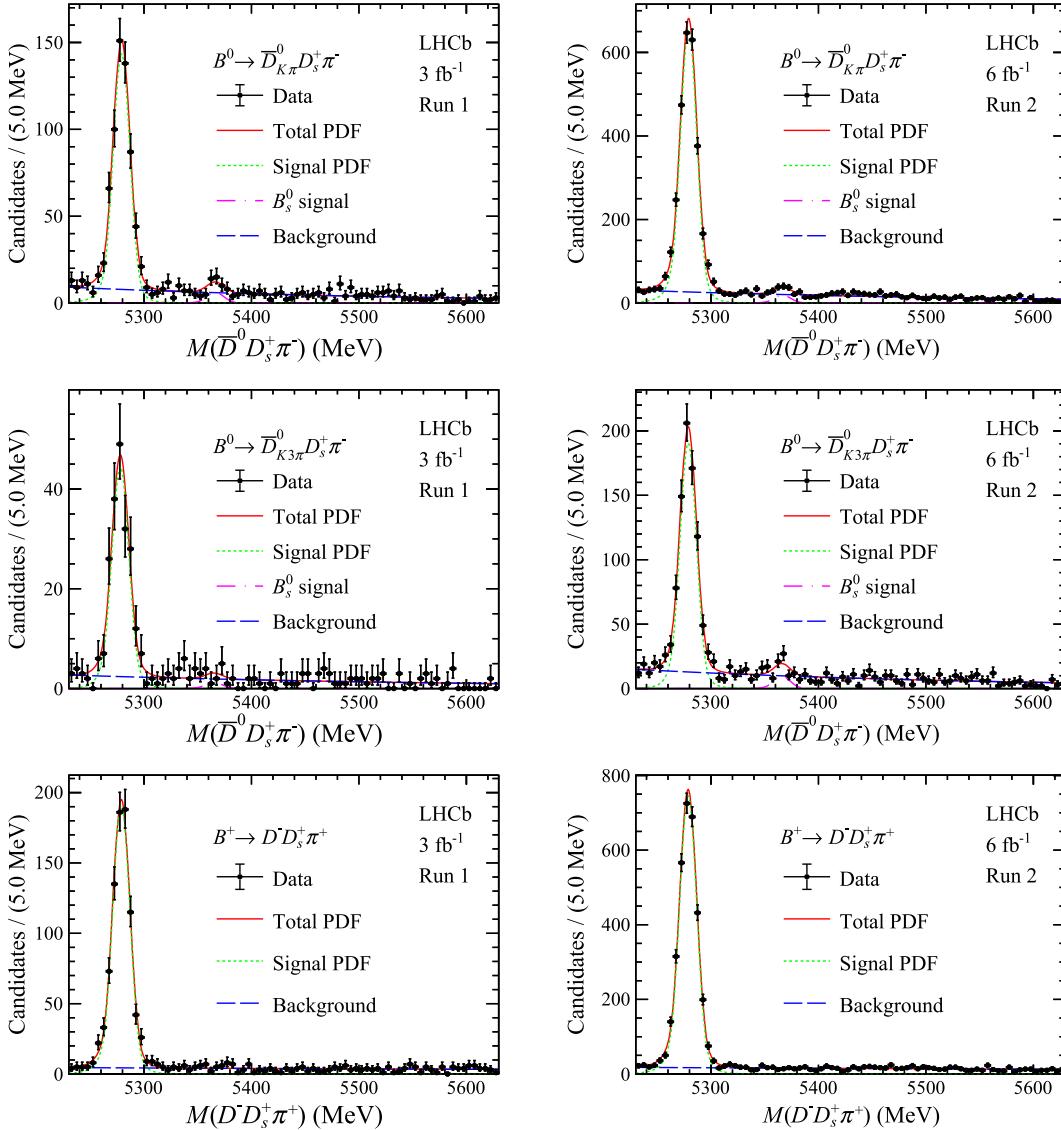

FIG. 2.   Invariant mass spectrum of the signal candidates, split by decay mode and run period. The data are overlaid with the results of the fit.

TABLE I.　Results of the fit parameters of invariant mass fit to the data samples. The uncertainties shown are statistical.

Decay	Parameter	Run 1	Run 2
$B^0 \to \overline{D}^0_{K\pi} D_s^+ \pi^-$	Signal yield	587 ± 27	2641 ± 57
	B_s^0 signal	25.3 ± 8.3	77 ± 15
	Background yield	421 ± 26	1440 ± 49
	Mean (MeV)	5279.12 ± 0.38	5279.16 ± 0.18
	Width (MeV)	7.89 ± 0.35	7.73 ± 0.17
	Exponential slope	$-(3.08 \pm 0.52) \times 10^{-3}$	$-(2.98 \pm 0.29) \times 10^{-3}$
$B^0 \to \overline{D}^0_{K3\pi} D_s^+ \pi^-$	Signal yield	185 ± 15	759 ± 32
	B_s^0 signal	4.9 ± 4.6	38 ± 11
	Background yield	136 ± 14	692 ± 33
	Mean (MeV)	5277.98 ± 0.70	5278.79 ± 0.34
	Width (MeV)	8.01 ± 0.59	7.72 ± 0.33
	Exponential slope	$-(2.56 \pm 0.90) \times 10^{-3}$	$-(3.03 \pm 0.41) \times 10^{-3}$
$B^+ \to D^- D_s^+ \pi^+$	Signal yield	798 ± 30	3123 ± 59
	Background yield	311 ± 21	1201 ± 40
	Mean (MeV)	5278.88 ± 0.33	5278.74 ± 0.16
	Width (MeV)	8.08 ± 0.30	8.05 ± 0.14
	Exponential slope	$-(0.82 \pm 0.61) \times 10^{-3}$	$-(0.90 \pm 0.31) \times 10^{-3}$

shared with the B^0 signal and the mean value $\mu_{B_s^0}$ is defined as $\mu_{B^0} + (m(B_s^0) - m(B^0))$, where the μ_{B^0} is the mean value of the Gaussian kernel of the B^0 signal PDF, and $m(B^0)$ and $m(B_s^0)$ are the known masses of the B^0 and B_s^0 mesons [7]. The tail parameters are fixed to the same values as the B^0 signal.

The results of the fit to the data samples are shown in Fig. 2. The values of the fitted parameters are listed in Table I, and Table II summarizes the signal yields, the number of candidates, and the purity inside the signal mass window used for the amplitude analysis.

V. ANALYSIS FORMALISM

The amplitude formalism and fit method of three-body $B \to abc$ decays, where abc denotes any sequence of $\bar{D}$, D_s^+, and π states, is established in this section.

TABLE II.　Signal and background yields inside the B mass signal window, together with the signal purity, split by run period and decay mode. The uncertainties shown are statistical.

Decay	Parameter	Run 1	Run 2
$B^0 \to \overline{D}^0_{K\pi} D_s^+ \pi^-$	Signal yield	564 ± 26	2534 ± 55
	Total candidates	633	2753
	Purity	89.1%	92.1%
$B^0 \to \overline{D}^0_{K3\pi} D_s^+ \pi^-$	Signal yields	177 ± 14	734 ± 31
	Total candidates	199	835
	Purity	88.9%	87.9%
$B^+ \to D^- D_s^+ \pi^+$	Signal yield	766 ± 29	2984 ± 57
	Total candidates	797	3143
	Purity	96.1%	94.9%

A. Amplitude model

The amplitude of the three-body $B \to \bar{D} D_s \pi$ decays is constructed following the isobar formalism [54–56], which is a coherent sum of quasi two-body amplitudes, either resonant or nonresonant,

$$\mathcal{A}(x; \Theta) = \sum c_i \cdot \mathcal{A}_i(x; \Theta_i), \qquad (2)$$

where c_i is a complex parameter for the ith contribution that is determined from data, x denotes variables calculated from the four-momenta of the final-state particles and Θ_i is a set of parameters used to describe the ith line shape. The amplitude of the ith quasi two-body decay to a and b (a, b represent any pair of D, D_s, π mesons) is

$$\mathcal{A}_i(x; \Theta_i) = T(\theta_{ab}) \cdot f(m_{ab}^2; \Theta_i), \qquad (3)$$

where $T(\theta_{ab})$ describes the angular distribution which depends on the spin J of the intermediate resonant state $R(ab)$. The helicity angle, θ_{ab}, is defined as the angle between the $R(ab)$ momentum direction in the B rest frame, and the momentum direction of a as determined in the $R(ab)$ rest frame. The definitions of $T(\theta_{ab})$ up to $J = 4$ are

$$T(\theta_{ab}) = \begin{cases} 1 & J = 0 \\ \cos\theta_{ab} & J = 1 \\ \cos^2\theta_{ab} - \frac{1}{3} & J = 2 \\ \cos^3\theta_{ab} - \frac{3}{5}\cos\theta_{ab} & J = 3 \\ \cos^4\theta_{ab} - \frac{30}{35}\cos^2\theta_{ab} + \frac{3}{35} & J = 4 \end{cases}. \qquad (4)$$

The function $f(M_{ab})$ is the line shape of the $R(ab)$ resonance where M_{ab} is the invariant mass of the pair. The complex relativistic Breit-Wigner (RBW) function is used as the default line shape,

$$f_{\text{RBW}}(M) = q(M)^{L_1}F(M,L_1) \cdot p(M)^{L_2}F(M,L_2)$$
$$\cdot \frac{1}{m_0^2 - M^2 - im_0\Gamma(M)}, \qquad (5)$$

where p is the momentum of particle a in the rest frame of the resonance $R(ab)$, and q denotes the momentum of $R(ab)$ in the B rest frame. The mass-dependent running width is

$$\Gamma(M) = \Gamma_0 \left(\frac{q(M)}{q_0}\right)^{2L_2+1} \frac{m_0}{M} F^2(M,L_2), \qquad (6)$$

where m_0 and Γ_0 are the mass and width of the resonance, respectively. The quantities p_0 and q_0 are these momenta evaluated when $M = m_0$. The orbital angular momentum between $R(ab)$ and c is denoted by L_1, while L_2 refers to the orbital angular momentum between particles a and b. Conservation of angular momentum implies that $L_1 = L_2 = J$. The Blatt-Weisskopf form-factor [57] $F(M,L)$ is parametrized as

$$F(M,L) = \begin{cases} 1 & L=0 \\ \sqrt{\frac{1+z_0^2(M)}{1+z_0^2}} & L=1 \\ \sqrt{\frac{9+3z^2(M)+z^4(M)}{9+3z_0^2+z_0^4}} & L=2 \\ \sqrt{\frac{225+45z^2(M)+6z^4(M)+z^6}{225+45z_0^2+6z_0^4+z_0^6}} & L=3 \end{cases} \qquad (7)$$

where $z(M) = pd$, $z_0 = p_0 d$, and d stands for the radial parameter, which is taken to be 3.0 GeV^{-1} by default for all resonances.

Nonresonant contributions are parametrized using an exponential function,

$$f_{NR} = \exp\left[-\alpha(M^2 - m_{\min}^2(D\pi))\right], \qquad (8)$$

where α is the slope parameter that is allowed to vary in the fit, and $m_{\min}^2(D\pi) = 4$ GeV^2 is an approximation of the $M^2(D\pi)$ lower threshold.

The RBW functions do not provide an adequate description of overlapping resonant states. Furthermore, the latest experimental [58] and theoretical [59] studies show that a simple BW line shape is not sufficient for the $\bar{D}_0^*(2300)$ resonance. A quasi-model-independent (QMI) parametrization [58] is used for the $D\pi$ S-wave, where the $M(D\pi)$ range is divided into k slices, and the line shape is replaced by a set of complex coefficients assigned to each slice, each free to vary in the fit. The real and imaginary parts are

independently interpolated using cubic splines. Details are given in Sec. VII.

B. Maximum likelihood fit

The normalized PDF for the signal is expressed as

$$P_{\text{sig}}^{\text{norm}}(x;\Theta) = \frac{1}{I_{\text{sig}}(\Theta)} \epsilon(x)|\mathcal{A}(x;\Theta)|^2. \qquad (9)$$

The normalization factor, $I_{\text{sig}}(\Theta)$, which is obtained by integrating over the phase space using simulated samples after full selection, and thus including $\epsilon(x)$ implicitly, can be expressed as

$$I_{\text{sig}}(\Theta) = \frac{\sum_j w_j |\mathcal{A}(x_j;\Theta)|^2}{\sum_j w_j}. \qquad (10)$$

The signal efficiency, $\epsilon(x)$, is obtained as described in Sec. VI. The w_j, also described in Sec. VI, are applied to the simulated events to correct for discrepancies between simulated samples and data, where the subscript j runs over all the events of the sample. The resolutions of the Dalitz plot coordinates are much smaller than the widths of the narrowest structures and thus related effects can be neglected. The total PDF is given by

$$\text{PDF}(x;\Theta) = f_{\text{sig}}P_{\text{sig}}^{\text{norm}}(x;\Theta) + f_{\text{bkg}}P_{\text{bkg}}^{\text{norm}}(x), \qquad (11)$$

where f_{sig} and f_{bkg} are the fractions of signal and background contributions, determined from the fit to the $m(DD_s\pi)$ invariant mass distributions, and $P_{\text{bkg}}^{\text{norm}}(x)$ is the normalized background PDF described in Sec. VI.

An amplitude fit is performed, minimizing the unbinned negative log-likelihood (NLL)

$$\text{NLL} \equiv -\ln\mathcal{L} = -\sum_j \ln \text{PDF}(x_j;\Theta). \qquad (12)$$

The signal efficiency map and background map are obtained separately for different samples. For the $B^0 \to \overline{D}^0 D_s^+ \pi^-$ decay, the different LHC run (1 or 2) and reconstruction channels ($B^0 \to \overline{D}^0_{K^+\pi^-} D_s^+\pi^-$, $B^0 \to \overline{D}^0_{K^+\pi^-\pi^-\pi^+} D_s^+\pi^-$) are fitted simultaneously. For the $B^+ \to D^- D_s^+ \pi^+$ decay, the run 1 and run 2 datasets are simultaneously fitted. Where isospin symmetry is imposed, the fit is performed simultaneously on all datasets.

The fit fraction $\mathcal{F}_i$ for a given contribution i is calculated from the fitted parameters, Θ_0, and is defined as

$$\mathcal{F}_i = \frac{\int |c_i \mathcal{A}_i(x;\Theta_{0,i})|^2 d\boldsymbol{x}}{\int |\mathcal{A}(x;\Theta_0)|^2 d\boldsymbol{x}}. \qquad (13)$$

The fit fractions do not necessarily add up to 1 due to interference effects between components. The interference term between any pair of components is defined as

$$\mathcal{F}_{ij} = \frac{\int 2\mathcal{R}(c_i c_j^* \mathcal{A}_i \mathcal{A}_j^*) \, d\boldsymbol{x}}{\int |\mathcal{A}(\boldsymbol{x}; \Theta_0)|^2 \, d\boldsymbol{x}}, \qquad (14)$$

$$m'(D\pi) = \frac{1}{\pi} \arccos \left(2 \times \frac{m(D\pi) - m_{D\pi}^{\min}}{m_{D\pi}^{\max} - m_{D\pi}^{\min}} - 1 \right), \quad (15)$$

and thus we have $\sum_i \mathcal{F}_i + \sum_{i<j} \mathcal{F}_{ij} = 1$.

$$\theta'(D\pi) = \frac{1}{\pi}\theta(D\pi). \qquad (16)$$

VI. SIGNAL EFFICIENCY AND BACKGROUND MODELS

The amplitude analysis is only sensitive to signal efficiency variations across the Dalitz plot, not the absolute efficiency. These are extracted for each dataset as a function of position in the square Dalitz plot (SDP), whose coordinates are defined by

Here $m(D\pi)$ is the invariant mass of the $D\pi$ combination, $m_{D\pi}^{\min}$ and $m_{D\pi}^{\max}$ are the kinematic limits of $m(D\pi)$ in $B \to DD_s\pi$ decays, and $\theta(D\pi)$ is the $D\pi$ helicity angle.

The efficiency maps across the SDP are evaluated from the simulated samples by kernel density estimation [45] and are shown in Fig. 3. The tracking efficiency and the efficiency of the trigger requirements have been corrected using control samples in data.

FIG. 3.   Signal efficiency maps for the $B^0 \to \bar{D}^0 D_s^+ \pi^-$, $\bar{D}^0 \to K^+\pi^-$ decays in (a) run 1 and (b) run 2; $B^0 \to \bar{D}^0 D_s^+ \pi^-$, $\bar{D}^0 \to K^+\pi^-\pi^-\pi^+$ decays in (c) run 1 and (d) run 2; $B^+ \to D^- D_s^+ \pi^+$ decays in (e) run 1 and (f) run 2. White regions are caused by $B^0 \to D^{*-} D_s^+$ veto.
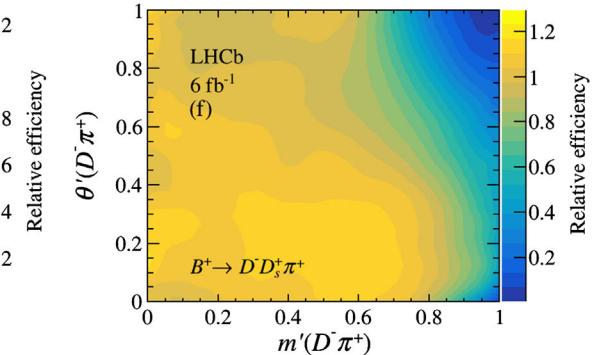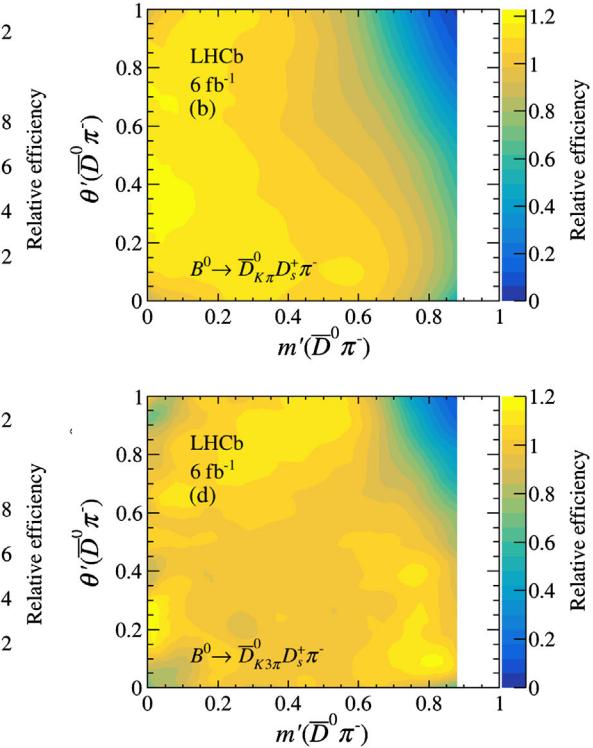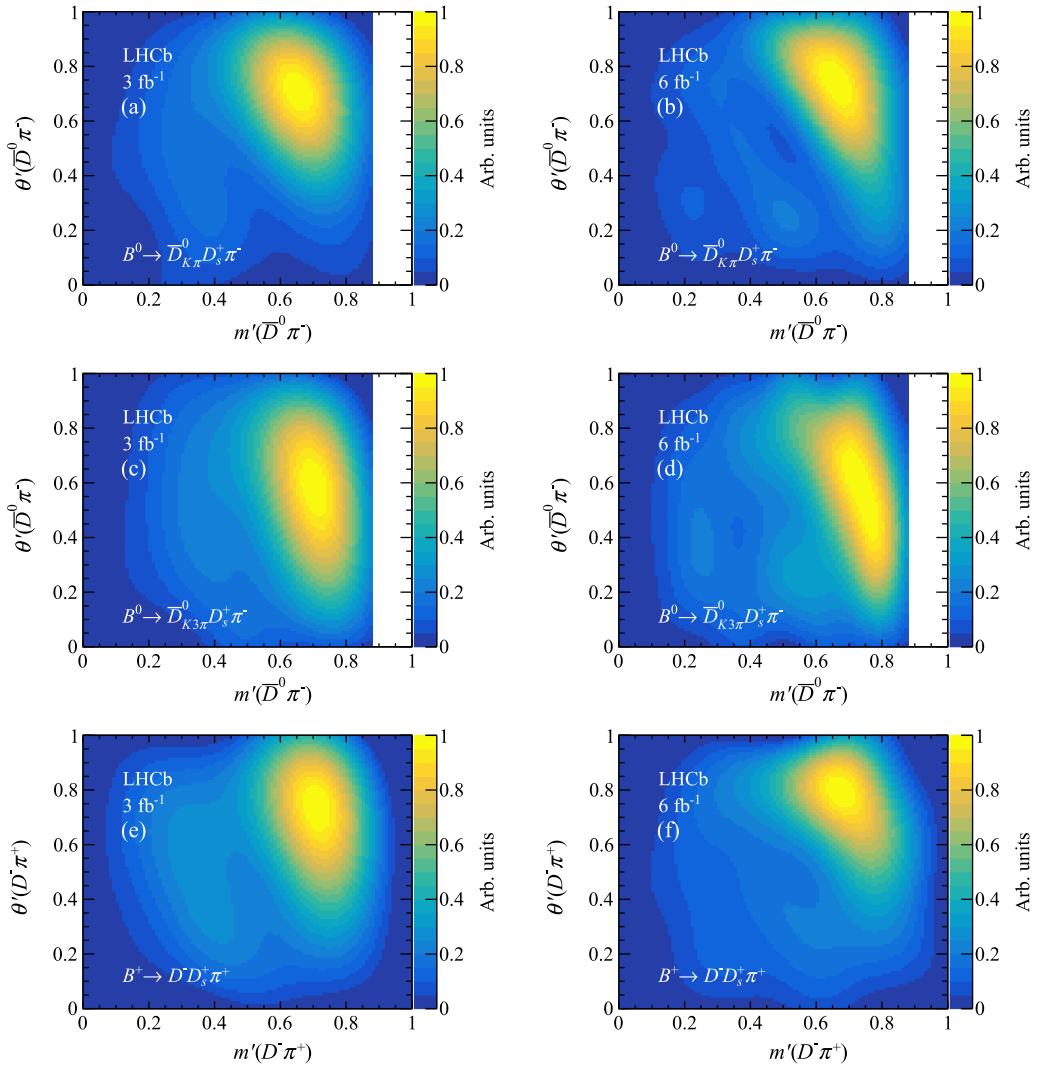
FIG. 4.　Distributions of the SPD background shapes for the $B^0 \to \overline{D}^0 D_s^+ \pi^-$, $\overline{D}^0 \to K^+\pi^-$ decays in (a) run 1 and (b) run 2; $B^0 \to \overline{D}^0 D_s^+ \pi^-$, $\overline{D}^0 \to K^+\pi^-\pi^-\pi^+$ decays in (c) run 1 and (d) run 2; $B^+ \to D^- D_s^+ \pi^+$ decays in (e) run 1 and (f) run 2. White regions are caused by $B^0 \to D^{*-} D_s^+$ veto.

The background distributions over the phase space are estimated using candidates in the B mass sidebands between [5450, 6000] MeV for the $B^0 \to \overline{D}^0 D_s^+ \pi^-$ decays and [5400, 6000] MeV for the $B^+ \to D^- D_s^+ \pi^+$ decays. The requirement on the BDT response is relaxed to increase the number of events in these regions as no significant change in the shapes of the distributions of sideband samples is observed. A Gaussian process extrapolation method [60] is applied to extrapolate the background Dalitz plot distribution into the B-meson signal region, in order to account for the correlations between the Dalitz variables and the invariant mass of the B candidates. The SDP distributions of the background shape for each dataset are shown in Fig. 4. The broad structures in the SDP distributions are related to the accumulation of combinatorial background with low pion momentum.

VII. AMPLITUDE ANALYSIS

Conventional resonances are only expected to decay to $\overline{D}^0 \pi^-$ and $D^- \pi^+$ final states in the $B^0 \to \overline{D}^0 D_s^+ \pi^-$ and the $B^+ \to D^- D_s^+ \pi^+$ decays, respectively. The straightforward way to perform the amplitude analysis is by including all the $D\pi$ resonances with natural spin-parity, as listed in Table III, in the fit model. It is called a model-dependent (MD) description. The result with the MD description is shown in Sec. VII G. The description of the $\bar{D}\pi$ S-wave distributions is improved by introducing a 0^+ $\bar{D}\pi$ QMI description, which accounts for both the broad spin-0 $\bar{D}\pi$ states and nonresonant components. The result with the QMI description is considered as the default, which is further discussed in this section.

TABLE III.　Resonances expected in $B^0 \to \overline{D}^0 D_s^+ \pi^-$ and $B^+ \to D^- D_s^+ \pi^+$ decays [7]. The masses and widths of resonances marked with # are shared for both the charged and neutral isospin partners.

Resonance	J^P	Mass (GeV)	Width (GeV)	Comments
$\overline{D}^*(2007)^0$	1^-	2.00685 ± 0.00005	$< 2.1 \times 10^{-3}$	Width set to be 0.1 MeV
$D^*(2010)^-$	1^-	2.01026 ± 0.00005	$(8.34 \pm 0.18) \times 10^{-5}$	
$\overline{D}_0^*(2300)$	0^+	2.343 ± 0.010	0.229 ± 0.016	#
$\overline{D}_2^*(2460)$	2^+	2.4611 ± 0.0007	0.0473 ± 0.0008	#
$\overline{D}_1^*(2600)^0$	1^-	2.627 ± 0.010	0.141 ± 0.023	#
$\overline{D}_3^*(2750)$	3^-	2.7631 ± 0.0032	0.066 ± 0.005	#
$\overline{D}_1^*(2760)^0$	1^-	2.781 ± 0.022	0.177 ± 0.040	#
$\overline{D}_J^*(3000)^0$	$?^?$	3.214 ± 0.060	0.186 ± 0.080	# $J^P = 4^+$ is assumed

A. Model including only $D\pi$ resonances

The basic fit model is defined by considering all known D^{**} states with natural spin-parity [7], as listed in Table III, except for the broad $D_0^*(2300)$ state. Their masses and widths are fixed to their default values. As described in Sec. VA, a QMI description of the $D\pi$ S-wave is used [58], with 11 spline points.[3] The first and last points are outside of the invariant mass range, and their amplitudes are fixed to zero. The other points are each assigned a complex coefficient that varies freely in the fit. Moreover, as the $\bar{D}^*(2007)^0$ mass is lower than the $D^-\pi^+$ mass threshold, the q_0 value in Eq. (6) would be imaginary. The q_0 value in this case is taken as the value calculated from $\bar{D}^*(2007)^0 \to \overline{D}^0\pi^0$ rather than $\bar{D}^*(2007)^0 \to D^-\pi^+$ in the default model. The $\bar{D}_J^*(3000)$ state was first observed in the $D^{*-}\pi^+$ decay mode, and its spin has not been determined yet [8]. A similar structure has been seen in $B^- \to D^+\pi^-\pi^-$ decays [58], with $J^P = 2^+$. In this analysis different J^P hypotheses for the $\bar{D}_J^*(3000)$ state are tested, either 1^-, 2^+, 3^-, or 4^+. In each case its mass and width are fixed to the corresponding default values [7]. The test results favor $J^P = 4^+$, which is used as the default.

The fit results, where only $D\pi$ resonances are included and the two decays are considered independently, are given in Figs. 5 and 6 for $B^0 \to \overline{D}^0 D_s^+ \pi^-$ and $B^+ \to D^- D_s^+ \pi^+$ decays, respectively. The $B^0 \to \overline{D}^0_{K^+\pi^-} D_s^+ \pi^-$, $B^0 \to \overline{D}^0_{K^+\pi^-\pi^-\pi^+} D_s^+ \pi^-$ decays are combined when plotting here and subsequently. A peaking structure at about 2.9 GeV is visible in the $M(D_s\pi)$ distribution of each decay, and is not well described by the included contributions. Furthermore, the addition of further D^* states up to $J^P = 4^+$ does not resolve the discrepancy. The normalized residuals of the fits are shown in Fig. 7. In the plot, the pull value in bin i is defined as $(N_{sig}^i - N_{fit}^i)/\sqrt{N_{sig}^i}$, where the N_{sig}^i and N_{fit}^i are

_____
[3][1.9, 2.0, 2.1, 2.2, 2.3, 2.4, 2.5, 2.6, 2.7, 2.9, 3.4] GeV.

the number of signal candidates and number of expected candidates from the fit result. The χ^2/ndf, where ndf is the number of degrees of freedom, 78.2/35 for $B^0 \to \overline{D}^0 D_s^+ \pi^-$, and 75.2/35 for $B^+ \to D^- D_s^+ \pi^+$, which also indicates the existence of a new resonance.

B. Model including $D_s^+\pi$ resonances

To improve the description of the $M(D_s^+\pi)$ distributions for the two decays, an additional $D_s^+\pi$ state is added to each decay, whose mass and width are free parameters, and different J^P assignments are tested. No relationship is assumed for the two $D_s^+\pi$ states. Both states with $J^P = 0^+$ give the best description of the data, while the $D_s^+\pi$ states with the other spin-parity are disfavored compared to the 0^+ hypothesis (see Sec. VII C). The distributions of $M(D_s^+\pi^-)$ in $B^0 \to \overline{D}^0 D_s^+ \pi^-$ and $M(D_s^+\pi^+)$ in $B^+ \to D^- D_s^+ \pi^+$ are shown in Fig. 8, where the two new $D_s^+\pi$ resonances, which are named as $T_{c\bar{s}0}^a(2900)^0$ and $T_{c\bar{s}0}^a(2900)^{++}$ following the convention in Ref. [61], are evident.

In the $M(D_s^+\pi^-)$ and $M(D_s^+\pi^+)$ distributions, both the peaks near 2.9 GeV and the dips near 3.0 GeV are better described by the presence of the new states and their interference with the existing D^* states. The masses and widths of the $T_{c\bar{s}0}^a(2900)^0$ and $T_{c\bar{s}0}^a(2900)^{++}$ states are listed in Table IV. Fit fractions are given in Tables V and VI for $B^0 \to \overline{D}^0 D_s^+ \pi^-$ and $B^+ \to D^- D_s^+ \pi^+$ decays, respectively. These results include the systematic uncertainties and corrections of fit bias, which are described in Sec. IX. The amplitudes and phases of the complex coefficients of the resonant contributions, relative to those of $\bar{D}_2^*(2460)$, are also displayed in Tables V and VI. The two-dimensional pull plots are given in Fig. 9. The χ^2/ndf is 43.2/31 and 63.0/31 for $B^0 \to \overline{D}^0 D_s^+ \pi^-$ and $B^+ \to D^- D_s^+ \pi^+$ decays, respectively. The distributions of Legendre polynomial weighted moments, together with the fit results with and without $T_{c\bar{s}0}^a(2900)^0$ and $T_{c\bar{s}0}^a(2900)^{++}$ states, are shown in Appendix; these also suggest the existence of the new
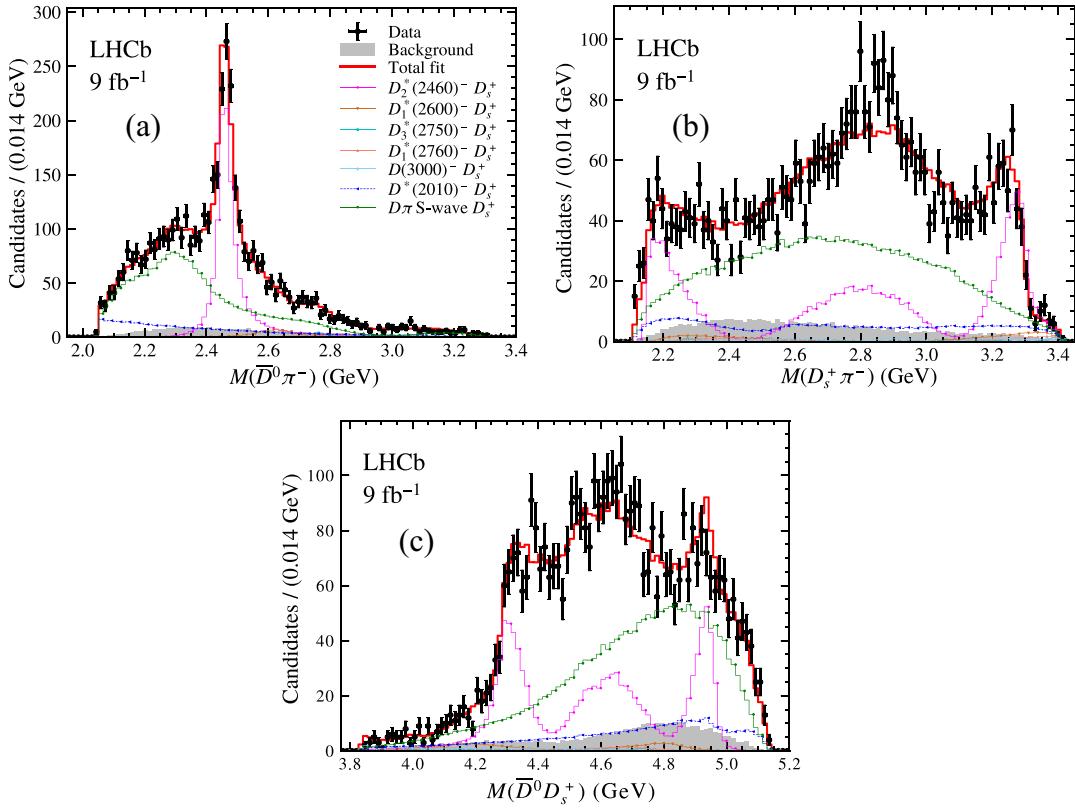
FIG. 5.   Invariant mass distributions (a) $M(\overline{D}^0\pi^-)$, (b) $M(D_s^+\pi^-)$, and (c) $M(\overline{D}^0 D_s^+)$ for the $B^0 \to \overline{D}^0 D_s^+\pi^-$ candidates compared with the fit results with only $D\pi$ resonances.
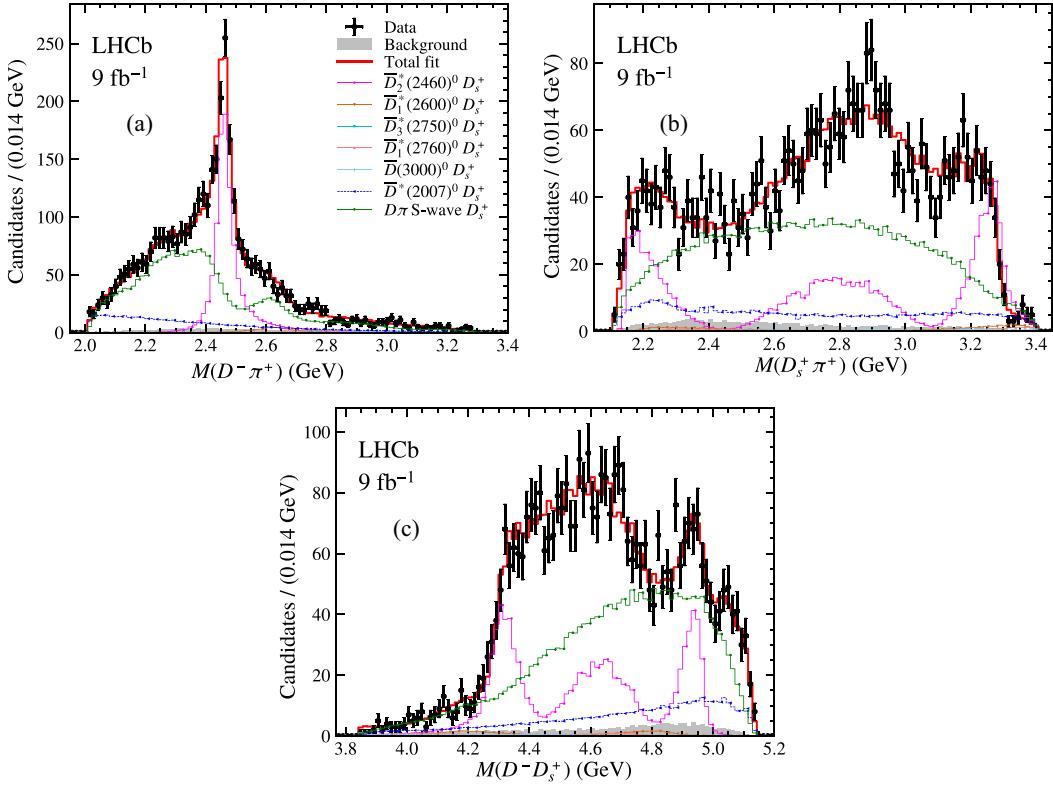

FIG. 6.   Invariant mass distributions of the (a) $M(D^-\pi^+)$, (b) $M(D_s^+\pi^+)$, and (c) $M(D^- D_s^+)$ for the $B^+ \to D^- D_s^+\pi^+$ candidates compared with the fit results with only $D\pi$ resonances.
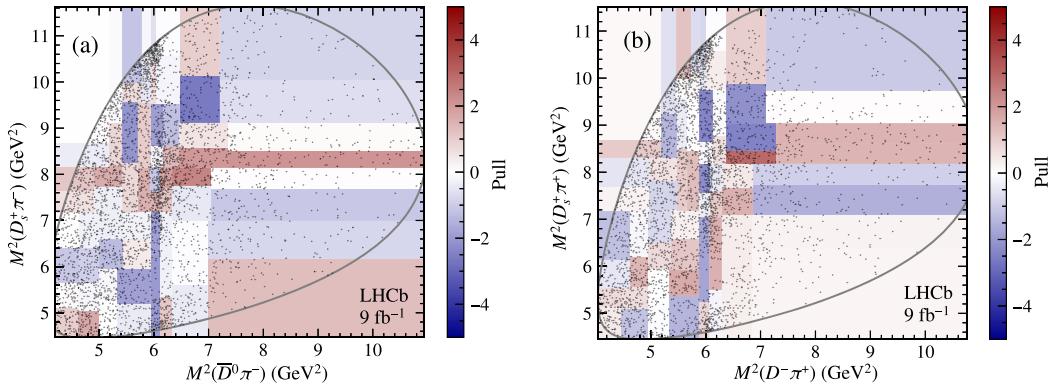
FIG. 7.   Two-dimensional pull plots of the fits to the (a) $B^0 \to \bar{D}^0 D_s^+ \pi^-$ and (b) $B^+ \to D^- D_s^+ \pi^+$ samples.

exotic states. The above model with a new 0^+ $T_{c\bar{s}0}^a(2900)$ is set as the default fit model.

C. Other models

Numerous additional resonances are tested to verify the stability of the default fit result and to better understand the system. First, the exotic $D_s^+\pi$ states with other spin-parity hypotheses are tested. The ΔLL values, with definition ΔLL=NLL$_{\text{Default}}$−NLL$_{\text{Other}}$, are summarized in Table VII. It is clear that at least one $D_s^+\pi$ exotic state is needed to

improve the value of NLL of the fit to each decay channel. The default model has the best fit quality, while the model with a spin-1 $D_s^+\pi$ state also provides reasonably good description. The data are tested against the spin 0 and spin 1 hypotheses for the $T_{c\bar{s}0}^a(2900)^0$ and $T_{c\bar{s}0}^a(2900)^{++}$ states. The results are shown in Sec. VII F and 0^+ is favored.

Second, the existence of extra $D\pi$, $D_s^+\pi$, and DD_s^+ states with natural spin-parity up to 3^- is explored when including the 0^+ $T_{c\bar{s}0}^a(2900)^0$ and $T_{c\bar{s}0}^a(2900)^{++}$ states. The masses and widths of the additional resonances are allowed
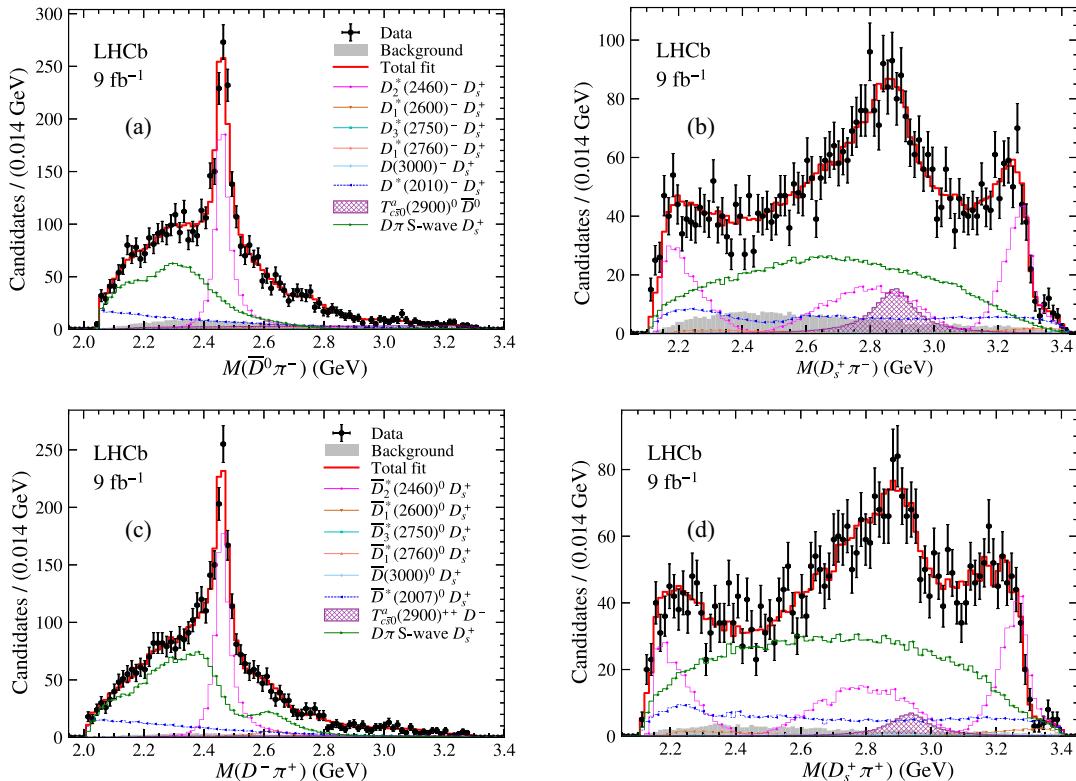
FIG. 8.   Projection of the fit result on (a) $M(D\pi)$ and (b) $M(D_s^+\pi)$ of $B^0 \to \bar{D}^0 D_s^+ \pi^-$ decays after including the $T_{c\bar{s}0}^a(2900)^0$ state, and on (c) $M(D\pi)$ and (d) $M(D_s^+\pi)$ of $B^+ \to D^- D_s^+ \pi^+$ decays after including the $T_{c\bar{s}0}^a(2900)^{++}$ state.

TABLE IV. Masses and widths of the $T_{c\bar{s}0}^a(2900)^0$ and $T_{c\bar{s}0}^a(2900)^{++}$ states. The values are corrected for biases. The first and second uncertainties are statistical and systematic, respectively.

Particle	Mass (GeV)	Width (GeV)
$T_{c\bar{s}0}^a(2900)^0$	$2.879 \pm 0.017 \pm 0.018$	$0.153 \pm 0.028 \pm 0.020$
$T_{c\bar{s}0}^a(2900)^{++}$	$2.935 \pm 0.021 \pm 0.013$	$0.143 \pm 0.038 \pm 0.025$

to vary freely in the fit. When considering an additional spin-0 or spin-1 $D_s^+\pi$ state for each decay, the mass of the new state converges near the $D_s^+\pi$ mass threshold. The resulting changes in the value of NLL are insignificant, corresponding to statistical significance of less than 2σ, and these states are not included in the default model.

The $D\pi$ states with natural spin-parities have been well investigated by the amplitude analyses of $B^0 \to \overline{D}^0\pi^+\pi^-$ [62], $B^+ \to D^-\pi^+\pi^+$ [58] and other topologically similar

TABLE V. Amplitude, phase, and fit fraction of each component in the $B^0 \to \overline{D}^0 D_s^+ \pi^-$ fit result. The values are corrected for fit biases. The first and second uncertainties are statistical and systematic, respectively.

Particle	Amplitude	Phase (rad)	Fraction (%)
$T_{c\bar{s}0}^a(2900)^0$	$0.223 \pm 0.044 \pm 0.048$	$-1.63 \pm 0.31 \pm 0.26$	$4.8 \pm 1.1 \pm 1.4$
$D^*(2010)^-$	$2.78 \pm 0.16 \pm 0.49$	$-2.90 \pm 0.11 \pm 0.10$	$14.0 \pm 1.5 \pm 1.8$
$D_2^*(2460)$	1	0	$22.1 \pm 1.1 \pm 0.6$
$D_1^*(2600)$	$0.207 \pm 0.046 \pm 0.040$	$0.36 \pm 0.24 \pm 0.19$	$1.12 \pm 0.55 \pm 0.49$
$D_3^*(2750)$	$0.174 \pm 0.046 \pm 0.062$	$-2.67 \pm 0.27 \pm 0.15$	$0.40 \pm 0.25 \pm 0.31$
$D_1^*(2760)$	$0.209 \pm 0.066 \pm 0.072$	$0.22 \pm 0.29 \pm 0.27$	$0.83 \pm 0.67 \pm 0.64$
$D_J^*(3000)$	$0.72 \pm 0.32 \pm 0.61$	$1.24 \pm 0.59 \pm 0.72$	$0.09 \pm 0.13 \pm 0.16$
$D\pi$ S-wave	$0.995 \pm 0.067 \pm 0.081$	$-0.983 \pm 0.069 \pm 0.077$	$39.5 \pm 2.6 \pm 2.9$

TABLE VI. Amplitude, phase, and fit fraction of each component in the $B^+ \to D^- D_s^+ \pi^+$ fit result. The values are corrected for fit biases. The first and second uncertainties are statistical and systematic, respectively.

Particle	Amplitude	Phase (rad)	Fraction (%)
$T_{c\bar{s}0}^a(2900)^{++}$	$0.139 \pm 0.046 \pm 0.037$	$-0.79 \pm 0.37 \pm 0.25$	$1.96 \pm 0.87 \pm 0.88$
$D^*(2007)^0$	$2.76 \pm 0.15 \pm 1.11$	$-3.03 \pm 0.10 \pm 0.43$	$15.7 \pm 1.5 \pm 2.0$
$D_2^*(2460)$	1	0	$22.2 \pm 1.1 \pm 0.7$
$D_1^*(2600)$	$0.228 \pm 0.050 \pm 0.086$	$-0.01 \pm 0.21 \pm 0.42$	$1.37 \pm 0.70 \pm 1.29$
$D_3^*(2750)$	$0.110 \pm 0.043 \pm 0.042$	$3.17 \pm 0.34 \pm 1.64$	$0.14 \pm 0.18 \pm 0.17$
$D_1^*(2760)$	$0.089 \pm 0.056 \pm 0.207$	$-0.98 \pm 0.78 \pm 2.23$	$0.10 \pm 0.33 \pm 1.57$
$D_J^*(3000)$	$1.74 \pm 0.34 \pm 1.87$	$1.31 \pm 0.32 \pm 2.07$	$0.65 \pm 0.27 \pm 0.82$
$D\pi$ S-wave	$1.276 \pm 0.066 \pm 0.093$	$-0.926 \pm 0.063 \pm 0.113$	$52.6 \pm 3.1 \pm 2.5$

TABLE VII. Tested fit models and the corresponding ΔLL value.

	ΔLL	
Model	$B^0 \to \overline{D}^0 D_s^+ \pi^-$	$B^+ \to D^- D_s^+ \pi^+$
Default model (One $D_s^+\pi$ state (0^+))	−	−
Variation of $D_s^+\pi$ states		
No $D_s^+\pi$ state	-35	-23
One $D_s^+\pi$ state (1^-)	-8	-15
One $D_s^+\pi$ state (2^+)	-27	-15
Two $D_s^+\pi$ states ($0^+ + 0^+$)	16	11
Two $D_s^+\pi$ states ($0^+ + 1^-$)	11	7
Additional $D\pi$ states		
1^- $D\pi$ state	5	6
2^+ $D\pi$ state	15	8
3^- $D\pi$ state	6	9
Additional DD_s^+ states		
0^+ DD_s^+ state	15	6
1^- DD_s^+ state	12	9
2^+ DD_s^+ state	6	9
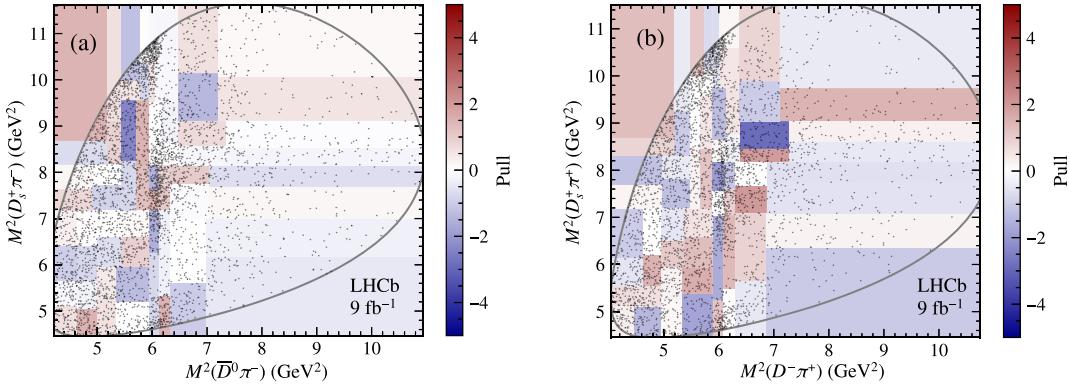
FIG. 9.   Two-dimensional pull plots of the fits to (a) $B^0 \to \overline{D}^0 D_s^+ \pi^-$ and (b) $B^+ \to D^- D_s^+ \pi^+$ samples after including the $T^a_{c\bar{s}0}(2900)^0$ and $T^a_{c\bar{s}0}(2900)^{++}$ states.

B-meson decays in LHCb [63–65] with large yields. No extra $D\pi$ state is expected to be observed in this analysis, which is consistent with the $D\pi$ results in Table VII. Additional DD_s^+ exotic states with natural spin-parities are also found to be disfavored, which is consistent with the previous results [28–30], where only 1^{+-} Z_{cs} states are observed.

D. Results related to excited D states

With the $T^a_{c\bar{s}0}(2900)^0$ and $T^a_{c\bar{s}0}(2900)^{++}$ states in place, the excited D states are investigated. Some tension in the measured mass of the $D_2^*(2460)$ state between inclusive results [8] and those obtained in amplitude fits [58,62–64] was seen previously. The mass and width of the $D_2^*(2460)$ states in the two decays are also investigated. The fit results in values of $m_0 = (2465.2 \pm 1.0)$ MeV, $\Gamma_0 = (38.7 \pm 2.5)$ MeV for the $D_2^*(2460)^-$ state and $m_0 = (2464.4 \pm 1.2)$ MeV, $\Gamma_0 = (44.6 \pm 2.8)$ MeV for the $D_2^*(2460)^0$ state. These results are in better agreement with earlier measurements in amplitude analyses. However they are also consistent with those obtained from inclusive results within 3σ when only considering statistical uncertainties [7].

The charged isospin partners of the $D_1^*(2600)^0$ and $D_J^*(3000)^0$ states have not yet been observed, their significances are estimated in the $B^0 \to \overline{D}^0 D_s^+ \pi^-$ decays based on the default fit model by fixing their masses and widths to the known values [7] and assuming the $D_J^*(3000)^0$ spin-parity to be 4^+. The statistical significance of the $D_1^*(2600)^-$, and $D_J^*(3000)^-$ resonances is estimated to be 4.8σ and 2.2σ, respectively. When the mass and width of the $D_1^*(2600)^-$ resonance are allowed to vary in the fit, they are determined to be $m_0 = (2640 \pm 51)$ MeV, $\Gamma_0 = (122 \pm 35)$ MeV which are consistent with the default values. The masses and widths of the $D_J^*(3000)^-$ state cannot be determined due to the limited sample size. While the significance of these states is small they are still included in the default fit for a conservative evaluation of the exotic contributions.

E. Search for $D_{s0}^*(2317)^0$ and $D_{s0}^*(2317)^{++}$ states

The nature of the $D_{s0}^*(2317)^+$ state is still in debate. Some theoretical models interpret the $D_{s0}^*(2317)^+$ state as an isoscalar $[cq\bar{s}\,\bar{q}]$ tetraquark state, and suggest searching for the isotriplet partners in the $D_s^+\pi^+$ and $D_s^+\pi^-$ final states [66–71]. The $B^0 \to \overline{D}^0 D_s^+ \pi^-$ and $B^+ \to D^- D_s^+ \pi^+$ decays are ideal for such studies.

However, in Sec. VII C, additional $D_s^+\pi$ exotic states with freely varying mass and width values, under different spin-parity hypotheses, are found to be insignificant. By assuming that the masses of the neutral and doubly charged partners are the same as that of the $D_{s0}^*(2317)^+$ state, the upper limit on fit fractions with three different scenarios is evaluated. The first scenario is that the natural width of the new $D_{s0}^*(2317)$ state is ignored. A Gaussian function is used to describe the line shape of the new state, of which the width represents the detector resolution. The second is that a Breit-Wigner function is added to model the $J^P = 0^+$, $D_s^+\pi$ state, of which the width is set to 3.8 MeV, the current upper limit on the $D_{s0}^*(2317)^+$ width [7]. No resolution effect is considered. The third is that an additional 0^+ $D_s^+\pi$ Breit-Wigner function, the width of which is set to be the same as the $T^a_{c\bar{s}0}(2900)^0$ and $T^a_{c\bar{s}0}(2900)^{++}$ states, is included in the fit model. The upper limits on the fit fractions of neutral and doubly charged $D_{s0}^*(2317)$ with different hypotheses at 90% C.L., which are all less than 1%, are summarized in Table VIII.

TABLE VIII.   Upper limit on the fit fractions of neutral and doubly charged $D_{s0}^*(2317)$ with different hypotheses at 90% C.L.

Hypothesis	$B^0 \to \overline{D}^0 D_s^+ \pi^-$	$B^+ \to D^- D_s^+ \pi^+$
(1)	0.063%	0.025%
(2)	0.053%	0.137%
(3)	0.861%	0.595%
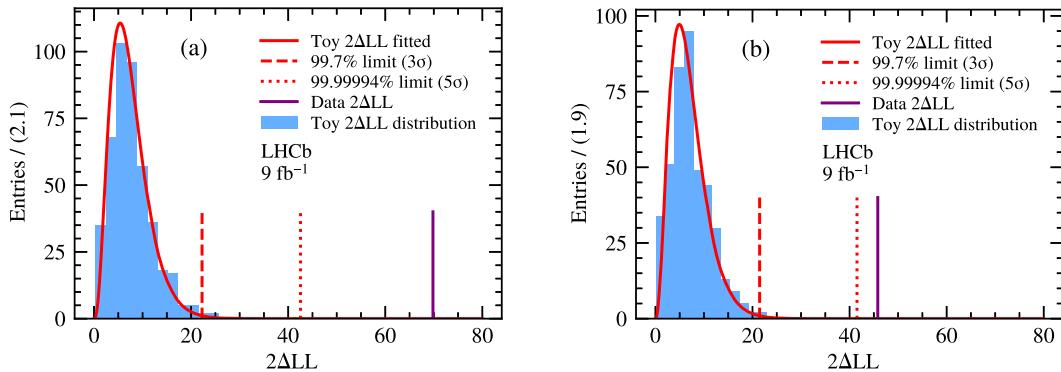
FIG. 10. Significance tests for the new $D_s\pi$ states in the (a) $B^0 \to \overline{D}^0 D_s^+ \pi^-$ and (b) $B^+ \to D^- D_s^+ \pi^+$ samples. The blue histogram is the distribution of $2\Delta\text{LL}$ and the red solid curve shows the fitted χ^2 PDF. The red dashed and dotted lines are the $2\Delta\text{LL}$ values corresponding to 3σ and 5σ, and the purple solid line is the $2\Delta\text{LL}$ measured in the data.

F. Significances, spin analysis, and Argand plot

Pseudoexperiments are carried out to determine the significance of the $T_{c\bar{s}0}^a(2900)^0$ and $T_{c\bar{s}0}^a(2900)^{++}$ states, accounting for the look-elsewhere effect [30,72]. The pseudoexperiments use data generated according to the fit results without the new $D_s^+\pi$ resonances, and the yield of each generated sample follows a Poisson distribution whose mean is the yield in the corresponding dataset. The pseudodatasets are fitted with the model with and without the $D_s^+\pi$ contributions. The difference in the value of $2\Delta\text{LL}$ between these two fits is obtained, and fitted with a χ^2 PDF. The distributions and fit results are shown in Fig. 10 for the two decays. The numbers of degrees of freedom after considering the look-elsewhere effect are found to be 7.39 ± 0.17 and 6.93 ± 0.17 for the $T_{c\bar{s}0}^a(2900)^0$ and $T_{c\bar{s}0}^a(2900)^{++}$ states, respectively, with the corresponding significances estimated to be 7.3σ and 5.3σ. After accounting for the systematic uncertainties discussed in Sec. IX, these are reduced to 6.6σ and 4.8σ.

The spin-parity values for the $T_{c\bar{s}0}^a(2900)^0$ and $T_{c\bar{s}0}^a(2900)^{++}$ states are also determined using pseudoexperiments. For each decay, 500 pseudoexperiments are generated based on the fit results with the 0^+ $D_s^+\pi$ state included, while another 500 pseudoexperiments are generated according to the fit results using a model assuming the 1^- spin hypothesis. Each pseudodataset is fitted in the same way as for data. The $2\Delta\text{LL}$ between the two fits is calculated, and the distributions of $2\Delta\text{LL}$ for the two sets of pseudoexperiments are shown in Fig. 11. The $2\Delta\text{LL}$ distribution of the pseudoexperiments with the 1^- $D_s^+\pi$ hypothesis is fitted with a Gaussian function, and the significance of the data disfavoring the 1^- hypothesis is evaluated to be 4.3σ for the $T_{c\bar{s}0}^a(2900)^0$ state and 4.2σ for the $T_{c\bar{s}0}^a(2900)^{++}$ state when no isospin relationship is imposed on the $D\pi$ or $D_s\pi$ components.

The Argand diagrams [7] of the $T_{c\bar{s}0}^a(2900)^0$ and $T_{c\bar{s}0}^a(2900)^{++}$ states are shown in Fig. 12. The Breit-Wigner function follows a counterclockwise circular path on the complex plane while contributions which are not
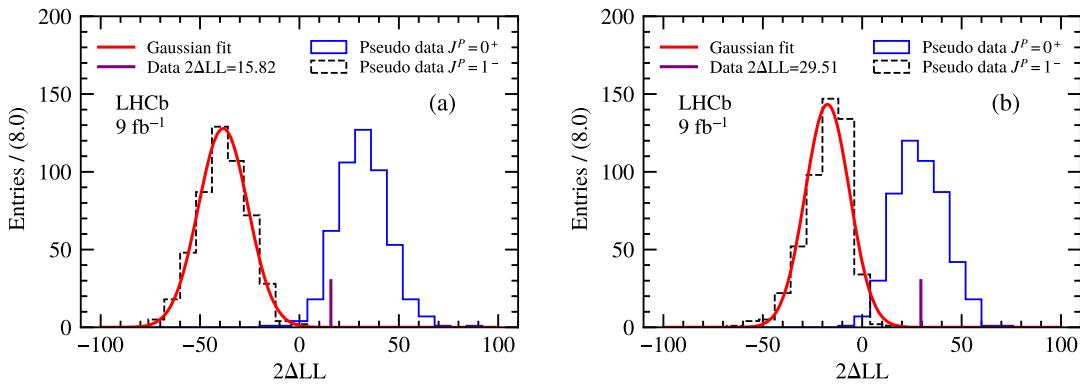
FIG. 11. Spin analysis of (a) $B^0 \to \overline{D}^0 D_s^+ \pi^-$ and (b) $B^+ \to D^- D_s^+ \pi^+$ decays. The blue solid and black dashed histograms are the distributions of the $2\Delta\text{LL}$ for the pseudoexperiments generated based on the fit results with 0^+ or 1^- $D_s^+\pi$ exotic state, respectively. The purple vertical line shows the $2\Delta\text{LL}$ value for the data fitted with the new $D_s^+\pi$ exotic state under the $J^P = 0^+$ and $J^P = 1^-$ hypotheses. The red curve is the result of a fit to the black dashed histogram with a Gaussian function.
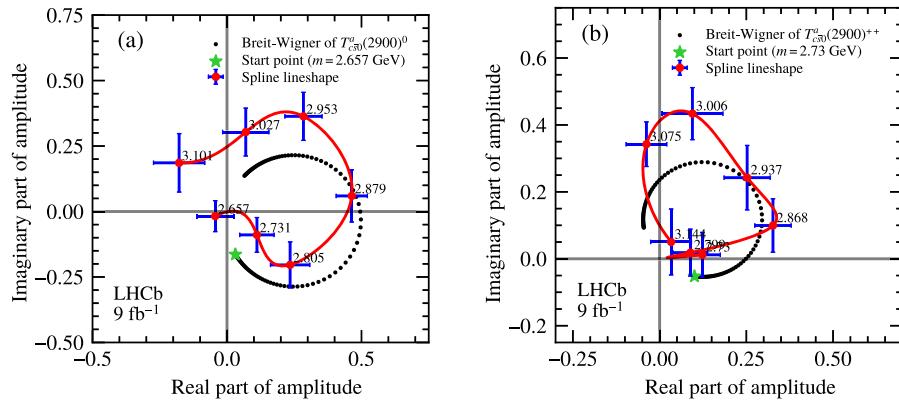
FIG. 12. Argand diagrams of the (a) $B^0 \to \bar{D}^0 D_s^+ \pi^-$ and (b) $B^+ \to D^- D_s^+ \pi^+$ decays. Black dots show the line shape of the $T_{c\bar{s}0}^a(2900)^0$ and $T_{c\bar{s}0}^a(2900)^{++}$ Breit-Wigner functions. The red solid line and blue error bars show the line shape and fit results of spline 0^+ $D_s^+\pi$ model in $T_{c\bar{s}0}^a(2900)^0$ and $T_{c\bar{s}0}^a(2900)^{++}$ mass region.

genuine resonances are expected to have a different shape. Seven spline points on $M_{D_s^+\pi}$ near the measured mass of the $T_{c\bar{s}0}^a(2900)^0$ and $T_{c\bar{s}0}^a(2900)^{++}$ states ($m \pm 1.5\Gamma$) are used to model these regions instead of Breit-Wigner functions. The complex parameters of all points are allowed to vary in the fit. The fitted parameters of the spline points, together with the $D_s^+\pi$ line shape are shown in Fig. 12. The spline line shape shows similar behavior as the Breit-Wigner distribution, which confirms the resonant character of the two new exotic states.

G. Model-dependent results

Instead of modeling the $D\pi$ S-wave with the QMI description, the amplitude fit with a fully MD description is carried out. In the MD description, the 0^+ QMI model is replaced by the RBW of the $D_0^*(2300)$ component together with a 0^+ nonresonant component, while the parameters of all the other resonances are set to be the same. The obtained parameters of the $T_{c\bar{s}0}^a(2900)^0$ and $T_{c\bar{s}0}^a(2900)^{++}$ states are summarized in Table IX and are consistent with those determined using the QMI model, within statistical uncertainties. Figures 13 and 14 show the fit results of the MD description of the $B^0 \to \bar{D}^0 D_s^+ \pi^-$ and $B^+ \to D^- D_s^+ \pi^+$ decays, respectively. The χ^2/ndf is 79.1/44 for the $B^0 \to \bar{D}^0 D_s^+ \pi^-$ decay and 114.7/44 for the $B^+ \to D^- D_s^+ \pi^+$ decay. As a comparison, the Argand diagrams of the MD and QMI 0^+ $D\pi$ components of the two decays are shown in Fig. 15. The MD and QMI spline points after 2.2 GeV are in good agreement. These results serve to validate the default fit.

VIII. SIMULTANEOUS $D\pi$ FIT MODEL

In the default fit model, all known D^{**} states with natural spin-parity [7] are included. However, their fit fractions, except those of the $D_2^*(2460)$ and $D_1^*(2600)$ states, are consistent with 0, as shown in Tables V and VI. Moreover, the parameters of the QMI 0^+ $D\pi$ spline points in the higher $D\pi$ mass region have large uncertainties due to the smaller sample size. To improve the precision and stability of the fit results, a simultaneous fit of the $B^0 \to \bar{D}^0 D_s^+ \pi^-$ and $B^+ \to D^- D_s^+ \pi^+$ decays is performed, as the two decays are related by isospin symmetry. In the simultaneous fit, all complex parameters of the D^{**} states are shared, except for the $\bar{D}^*(2007)^0$ and $D^*(2010)^-$ states allowing for small isospin symmetry breaking effects near the $D\pi$ mass threshold. The simultaneous fit results with only $D\pi$ states are shown in Ref. [31]. The description of the mass spectra is consistent with the separate fit as shown in Sec. VII A, which supports the feasibility to perform simultaneous fit for the two decays.

The fit results are shown in Fig. 16. As separate fit, neutral, and doubly charged $D_s^+\pi$ states are needed to describe the data well, where their parameters are set to be different. The masses, widths, and fit fractions of the $T_{c\bar{s}0}^a(2900)^0$ and $T_{c\bar{s}0}^a(2900)^{++}$ states after considering the systematic uncertainties and possible fit bias, which are summarized in Tables X and XI, show good agreement with the separate fit result, with significant improvement on the relative statistical uncertainties. The total χ^2/ndf is evaluated to be 140.3/89.

TABLE IX. Masses, widths and fit fractions of the $T_{c\bar{s}0}^a(2900)^0$ and $T_{c\bar{s}0}^a(2900)^{++}$ states obtained from the MD fit.

Model	ΔLL	Mass (GeV)	Width (GeV)	Fraction (%)
$T_{c\bar{s}0}^a(2900)^0$	70.1	2.871 ± 0.012	0.135 ± 0.025	3.0 ± 0.5
$T_{c\bar{s}0}^a(2900)^{++}$	33.2	2.922 ± 0.014	0.161 ± 0.033	2.0 ± 0.5
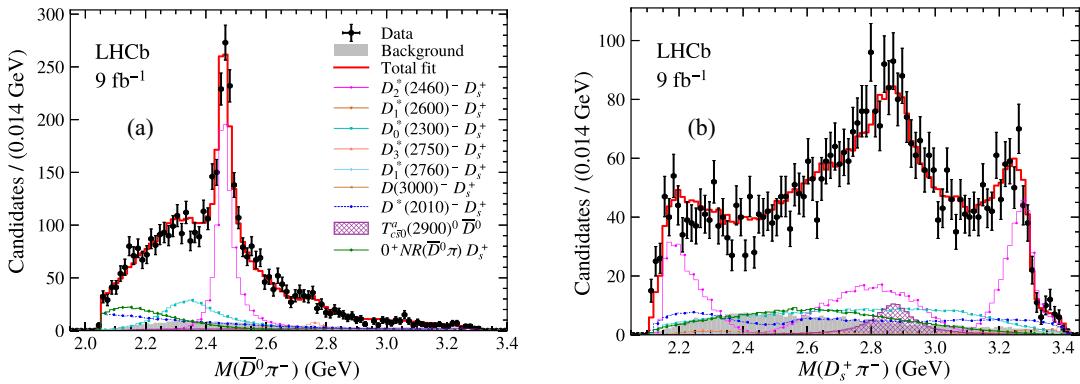
FIG. 13.   The MD description of the (a) $M(\overline{D}^0\pi^-)$ and (b) $M(D_s^+\pi^-)$ distributions for the $B^0 \to \overline{D}^0 D_s^+ \pi^-$ decays.
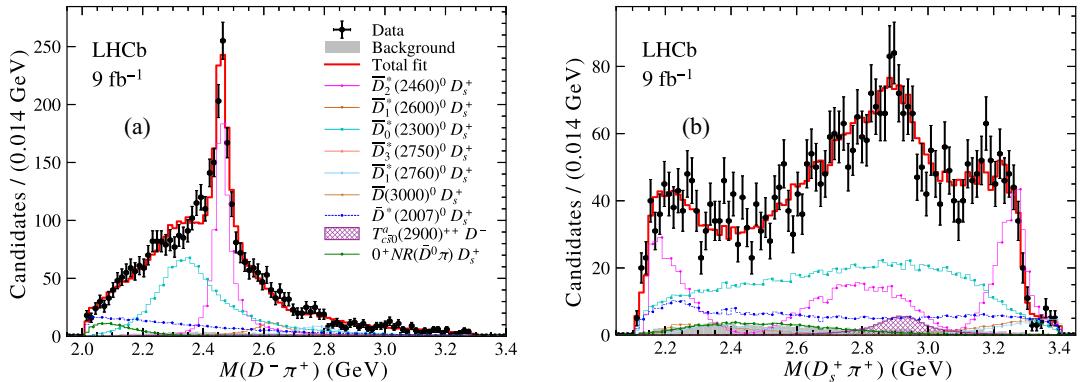
FIG. 14.   The MD description of the (a) $M(D^-\pi^+)$ and (b) $M(D_s^+\pi^+)$ distributions for the $B^+ \to D^- D_s^+ \pi^+$ decays.

The *ndf* of the $T_{c\bar{s}0}^a(2900)^0$ and $T_{c\bar{s}0}^a(2900)^{++}$ states in the simultaneous $D\pi$ fit model are evaluated to be 7.29 ± 0.18 and 8.57 ± 0.17 in the same way as described in Sec. VII F, with the corresponding significances estimated to be 9.0σ and 7.4σ, respectively. After accounting for the systematic uncertainties discussed in Sec. IX, these are reduced to 8.0σ and 6.5σ. The constraints on the $D\pi$ contributions using isospin symmetry lead to higher significance, as expected.

To estimate the isospin-breaking effects between the $T_{c\bar{s}0}^a(2900)^0$ and $T_{c\bar{s}0}^a(2900)^{++}$ states, the mass difference, $\Delta M = M(T_{c\bar{s}0}^a(2900)^{++}) - M(T_{c\bar{s}0}^a(2900)^0)$, and width difference, $\Delta\Gamma = \Gamma(T_{c\bar{s}0}^a(2900)^{++}) - \Gamma(T_{c\bar{s}0}^a(2900)^0)$, are evaluated to be $28 \pm 20 \pm 12$ MeV and $15 \pm 39 \pm 16$ MeV, respectively, where the first and second uncertainties are statistical and systematic. The statistical uncertainties in ΔM and $\Delta\Gamma$ are evaluated using pseudoexperiments to
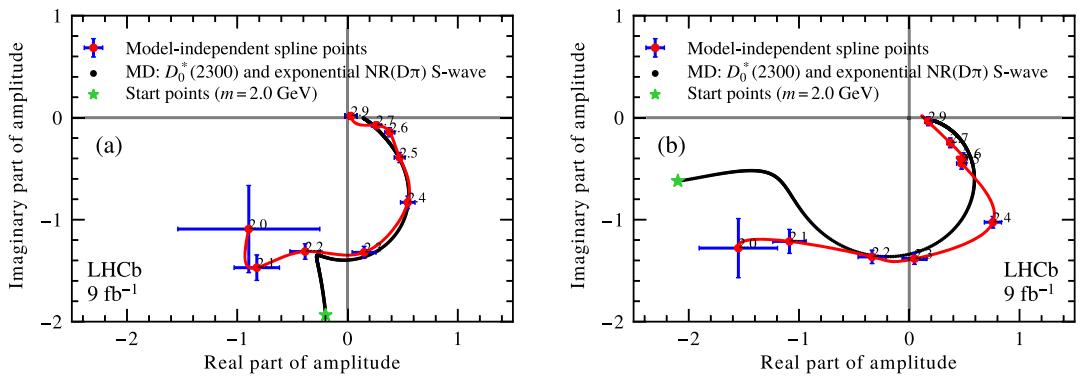
FIG. 15.   Argand diagrams of the MD and QMI 0^+ $D\pi$ components of the (a) $B^0 \to \overline{D}^0 D_s^+ \pi^-$ and (b) $B^+ \to D^- D_s^+ \pi^+$ decays. The red solid line and blue error bars show the line shape and fit results of QMI 0^+ $D\pi$ spline model, while the black line is the line shape of the MD 0^+ $D\pi$ component.
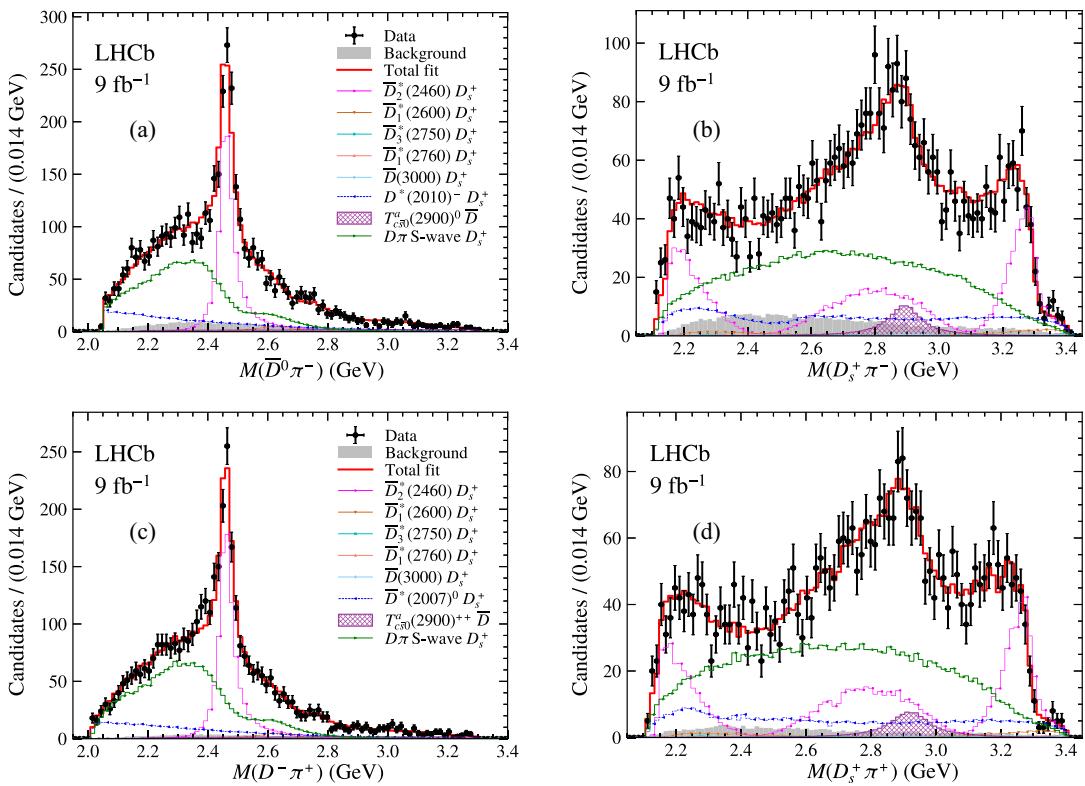
FIG. 16. Fit result of simultaneous $D\pi$ fit model, the (a) $M(D\pi)$ and (b) $M(D_s^+\pi)$ distributions of $B^0 \to \bar{D}^0 D_s^+ \pi^-$ decays after including the $T_{c\bar{s}0}^a(2900)^0$ state; the (c) $M(D\pi)$ and (d) $M(D_s^+\pi)$ distributions of $B^+ \to D^- D_s^+ \pi^+$ decays after including the $T_{c\bar{s}0}^a(2900)^{++}$ state.

TABLE X. Masses and widths of the $T_{c\bar{s}0}^a(2900)^0$ and $T_{c\bar{s}0}^a(2900)^{++}$ states. The values are corrected for biases as described in the text. The first and second uncertainties are statistical and systematic, respectively.

Particle	Mass (GeV)	Width (GeV)
$T_{c\bar{s}0}^a(2900)^0$	$2.892 \pm 0.014 \pm 0.015$	$0.119 \pm 0.026 \pm 0.013$
$T_{c\bar{s}0}^a(2900)^{++}$	$2.921 \pm 0.017 \pm 0.020$	$0.137 \pm 0.032 \pm 0.017$

TABLE XI. Amplitude, phase, and fit fraction of each component in the simultaneous $D\pi$ fit model. The values are corrected based on the results of pseudoexperiments. The first and second uncertainties are the statistical and systematic, respectively.

Particle	Amplitude	Phase (rad)	B^0 Fraction (%)	B^+ Fraction (%)
$T_{c\bar{s}0}^a(2900)^0$	$0.139 \pm 0.032 \pm 0.028$	$-1.39 \pm 0.26 \pm 0.29$	$2.48 \pm 0.67 \pm 0.77$	$\cdots$
$T_{c\bar{s}0}^a(2900)^{++}$	$0.143 \pm 0.036 \pm 0.031$	$-1.19 \pm 0.29 \pm 0.38$	$\cdots$	$2.25 \pm 0.67 \pm 0.77$
$D^*(2007)^0$	$2.65 \pm 0.14 \pm 1.06$	$-2.98 \pm 0.07 \pm 0.32$	$\cdots$	$14.7 \pm 1.3 \pm 2.7$
$D^*(2010)^-$	$2.94 \pm 0.15 \pm 0.49$	$-2.92 \pm 0.07 \pm 0.28$	$15.8 \pm 1.3 \pm 2.4$	$\cdots$
$D_2^*(2460)$	1	0	$22.38 \pm 0.88 \pm 0.60$	$22.35 \pm 0.91 \pm 0.71$
$D_1^*(2600)$	$0.223 \pm 0.033 \pm 0.052$	$0.15 \pm 0.16 \pm 0.26$	$1.35 \pm 0.40 \pm 0.59$	$1.37 \pm 0.42 \pm 0.62$
$D_3^*(2750)$	$0.151 \pm 0.031 \pm 0.035$	$-2.81 \pm 0.20 \pm 0.57$	$0.31 \pm 0.14 \pm 0.17$	$0.31 \pm 0.15 \pm 0.17$
$D_1^*(2760)$	$0.121 \pm 0.043 \pm 0.164$	$-0.19 \pm 0.35 \pm 0.98$	$0.28 \pm 0.25 \pm 1.48$	$0.28 \pm 0.26 \pm 1.53$
$D_J^*(3000)$	$1.44 \pm 0.24 \pm 1.20$	$1.41 \pm 0.23 \pm 1.29$	$0.45 \pm 0.16 \pm 0.38$	$0.45 \pm 0.16 \pm 0.37$
$D\pi$ S-wave	$1.141 \pm 0.044 \pm 0.081$	$-0.966 \pm 0.044 \pm 0.083$	$45.5 \pm 2.1 \pm 3.3$	$48.3 \pm 2.2 \pm 3.5$

account for the correlations, and some of the systematic uncertainties are canceled. The masses and widths of the two exotic states are consistent with each other within 1σ, which confirms that they are related by isospin symmetry.

The full simultaneous fit, where the parameters of the $T^a_{c\bar{s}0}(2900)^0$ and $T^a_{c\bar{s}0}(2900)^{++}$ states are shared in the fit, is also performed, and described in a separate Letter [31].

IX. SYSTEMATIC UNCERTAINTIES

The sources of systematic uncertainty fall into two categories: experimental and those related to the amplitude model. In the first category there are effects related to the fixed signal yields of B candidates, the models of the background distributions, and the signal efficiency computation. Those arising from the amplitude model are mainly due to the fixed parameters of the model. The total systematic uncertainty is found by summing these in quadrature.

The signal yields in the amplitude analysis are taken from the results of the fits to the invariant mass distributions of B candidates. To determine the systematic uncertainty, the signal yield of each dataset is varied according to a Gaussian distribution whose width corresponds to a signal-yield uncertainty that includes uncertainties due to the modeling of the invariant mass distribution. The amplitude fit is repeated with the new signal yields and the rms value of each fit parameter is taken as the systematic uncertainty.

Backgrounds are modeled using a Gaussian process extrapolation method [60] according to sideband distributions. To evaluate the associated systematic uncertainty, the background model is replaced by the result of a kernel density estimation [45] applied to the Dalitz-plot distributions of the sideband samples. The deviations of the fit parameters from the default result are taken as the associated systematic uncertainties.

Knowledge of the signal efficiency variation over the Dalitz plot is limited by four effects: uncertainty in the PID response, trigger efficiency calibration uncertainties, signal efficiency determination, and simulation sample size. The systematic uncertainty due to the PID calibration is estimated by regenerating the PID responses with a perturbed kernel density estimation [45], extracting the efficiencies, and repeating all the fitting procedures. For the trigger efficiency calibration effect, a conservative systematic uncertainty is determined by repeating all the fitting procedures with the signal efficiency maps without any trigger efficiency correction. The systematic uncertainty related to the signal efficiency determination is estimated by performing the amplitude analysis with the efficiency maps obtained using an alternative kernel density estimation. The deviations of the fit parameters in each fit are taken to be the systematic uncertainties.

The systematic uncertainty due to the limited size of the simulated samples is determined by generating 200 samples following the bootstrap method [73], where the simulated candidates after all the selection criteria are allowed to be picked multiple times. The efficiencies are then extracted from each bootstrapped sample and applied in the amplitude analysis. The rms of each fit parameter in these fits is taken as the systematic uncertainty.

The fixed parameters in the amplitude analysis include the radius d in the Blatt-Weisskopf form factor, and the parameters of the $D\pi$ line shapes. The systematic uncertainty associated to d is evaluated by setting d to 1.5 GeV^{-1} and 4.5 GeV^{-1}. The largest difference compared to the default results is assigned as the systematic uncertainty. The fixed $D\pi$ parameters consist of the masses and widths of all the D^* states in Table III, the choice of the QMI spline points, the constant q_0 in the $D^*(2007)^0$ state line shape, and the spin hypothesis of $D_J(3000)$. The amplitude fits are performed several times, with one or more parameters changed. The fixed masses and widths of all the D^* states are allowed to vary one at a time in the fit but are constrained by a Gaussian function within uncertainties in their default values [7]. The positions of the QMI spline points are chosen empirically in the default fit, and shifted by ± 10 MeV in the amplitude analysis. The systematic uncertainty from the number of the QMI spline points is also explored by adding a new point at $M(D\pi) = 2.35$ GeV to try to improve the model description near the $\overline{D}^*_0(2300)$ mass region, or by removing the point at $M(D\pi) = 2.6$ GeV as there is no 0^+ $D\pi$ state observed in this region. The q_0 of the $D^*(2007)^0$ state is taken as the q_0 of the $D^*(2007)^0 \to D^0\pi^0$ decay in the default fit, and replaced by a value calculated from the $D^*(2007)^0$ effective mass [58]. The spin of the $D_J(3000)$ state is found to be 4^+ in the default fit, and altered to 2^+, the result measured in Ref. [58]. The deviations of the results between each fit and the default fit are summed in quadrature and taken as the systematic uncertainty.

Possible fit biases are investigated using pseudoexperiments, and used to correct the results. For each dataset, 500 samples are generated according to the default fit results, where the yield of each is sampled from a Poisson distribution whose mean value is the number of B candidates in the corresponding dataset. The fit parameters of the pseudodata are then extracted using the default fit model. The residual distributions ($\mu_{\text{pseudo}} - \mu_{\text{default}}$) and pull distributions ($\mu_{\text{pseudo}} - \mu_{\text{default}})/\sigma_{\text{pseudo}}$ are extracted from the pseudoexperiments and default fit result, and used to correct the fit results. Here the μ_{pseudo} and σ_{pseudo} are the mean values and uncertainties in the pseudoexperiments. Both the residual distributions and pull distributions of each parameter are fitted with a Gaussian function. The mean value of the residual distribution from the Gaussian fit is used to correct the mean value of the parameter, while the width of the pull distribution is used to scale the statistical uncertainty. The results are summarized in Tables IV, V, and VI. The systematic uncertainties of the simultaneous $D\pi$ fit

are also evaluated in the same way, and summarized in Tables X and XI.

X. CONCLUSION

Amplitude analyses of $B^0 \to \overline{D}^0 D_s^+ \pi^-$ and $B^+ \to D^- D_s^+ \pi^+$ decays are performed for the first time using LHCb pp collision data taken at center-of-mass energies of 7, 8, and 13 TeV, corresponding to a total integrated luminosity of 9 fb^{-1}. In total, signal yields of 4009 ± 70 and 3750 ± 64 candidates are obtained from the $B^0 \to \overline{D}^0 D_s^+ \pi^-$ and $B^+ \to D^- D_s^+ \pi^+$ decays, respectively.

When all known $D\pi$ resonances with spin-parities of $1^-, 2^+, 3^-,$ and 4^+ [7] are included, along with a QMI spline model to describe the 0^+ $D\pi$ distributions, the results show that the $D_s^+ \pi$ invariant-mass distributions are not well described. To improve the model description, a 0^+ $D_s^+ \pi$ resonance is added to each decay mode. The masses and widths of the two resonances are determined to be

$$T_{c\bar{s}0}^a(2900)^0\colon M = (2.879 \pm 0.017 \pm 0.018) \text{ GeV},$$
$$\Gamma = (0.153 \pm 0.028 \pm 0.020) \text{ GeV},$$
$$T_{c\bar{s}0}^a(2900)^{++}\colon M = (2.935 \pm 0.021 \pm 0.013) \text{ GeV},$$
$$\Gamma = (0.143 \pm 0.038 \pm 0.025) \text{ GeV},$$

where the first uncertainty is statistical and the second systematic. The significances, accounting for the look-elsewhere effect and systematic uncertainties, of the exotic $T_{c\bar{s}0}^a(2900)^0$ and $T_{c\bar{s}0}^a(2900)^{++}$ states are 6.6σ and 4.8σ, respectively.

A simultaneous $D\pi$ amplitude fit assuming isospin symmetry in the $B^0 \to \overline{D}^0 D_s^+ \pi^-$ and $B^+ \to D^- D_s^+ \pi^+$ decays is also performed to provide better control on the contributions from $D\pi$ resonances, especially the 0^+ $D\pi$ spline model, and to improve the precision of the measured parameters of exotic states. The masses and widths of the two resonances in the simultaneous $D\pi$ fit are measured to be

$$T_{c\bar{s}0}^a(2900)^0\colon M = (2.892 \pm 0.014 \pm 0.015) \text{ GeV},$$
$$\Gamma = (0.119 \pm 0.026 \pm 0.013) \text{ GeV},$$
$$T_{c\bar{s}0}^a(2900)^{++}\colon M = (2.921 \pm 0.017 \pm 0.020) \text{ GeV},$$
$$\Gamma = (0.137 \pm 0.032 \pm 0.017) \text{ GeV},$$

with the significances evaluated to be 8.0σ and 6.5σ for the $T_{c\bar{s}0}^a(2900)^0$ and $T_{c\bar{s}0}^a(2900)^{++}$ states, including systematic uncertainties. The mass and width differences between $T_{c\bar{s}0}^a(2900)^{++}$ and $T_{c\bar{s}0}^a(2900)^0$ are evaluated to be

$$\Delta M = (28 \pm 20 \pm 12) \text{ MeV},$$
$$\Delta \Gamma = (15 \pm 39 \pm 16) \text{ MeV},$$

based on simultaneous $D\pi$ amplitude fit, and consistent with zero. A simultaneous fit with the parameters of the $D_s^+ \pi$ exotic states shared is also performed and described in a separate Letter [31]. All the results of the different fit scenarios show good agreement.

This is the first observation of an isospin triplet of manifestly exotic mesons with four different quark flavors. The masses and widths of the two states are consistent with the $X_0(2900)$ and $X_1(2900)$ states [3,4], but have an opposite strangeness number. No hint of a DD_s^+ structure is observed in the analysis. With the significantly larger data samples that will be collected by the upgraded LHCb detector in the coming years, the nature of the isospin triplet of exotic mesons, and the existence of the possible $D_s^+ \pi$ exotic states with $J^P = 1^-$ in the same region, will be further explored.

APPENDIX: MOMENTS ANALYSIS RESULTS

Moments analysis is useful to suggest possible resonant structures in the decay. The formulation and the results are provided in this section.

The Legendre polynomial of a certain order k, as expressed in Eq. (A1), is used to weight the data,

$$P_k(x) = \sqrt{\frac{2k+1}{2}} 2^k \sum_{j=0}^{k} x^j \binom{k}{j} \binom{\frac{k+j-1}{2}}{k}. \quad \text{(A1)}$$

For example, when focusing on the resonant structures of the $D\pi$ channel, the variable x in this case would be the helicity variable in that decay chain, namely $\cos\theta_D^{D\pi}$. Therefore, the total amplitude modified by the order-k Legendre polynomial can be expressed as

$$\langle Y_k \rangle = \sum_{i=1}^{N} w_i P_k(\cos\theta_D^{D\pi}), \quad \text{(A2)}$$

where w_i is the original weight for the data point i.

By analytical calculation, the relationship between the Legendre-weighted total amplitude $\langle Y_k \rangle$ and combination of different orders of partial waves [58] can be bridged. Considering the existence of partial waves with the first J orders of orbital momentum, only $\langle Y_k \rangle$ of k up to $2J$ are nonzero. The weighted distributions can be visualized on the $M^2(D\pi)$ axis, which can be helpful to distinguish the structures from different ordered partial waves. The moments on the two axes, $M^2(D\pi)$, $M^2(D_s\pi)$, are shown up to the eighth order. The results, which are shown in Figs. 17–20, are taken from the separate fits to $B^0 \to \overline{D}{}^0 D_s^+ \pi^-$ and $B^+ \to D^- D_s^+ \pi^+$, where the data are background subtracted and efficiency corrected.

FIG. 17. Moments analysis of $B^0 \to \overline{D}{}^0 D_s^+ \pi^-$ on $M^2(\overline{D}{}^0\pi^-)$. The black points indicate the data, while the blue and red histogram indicate the fit results without and with the $T_{c\bar{s}0}^a(2900)$ states separately.
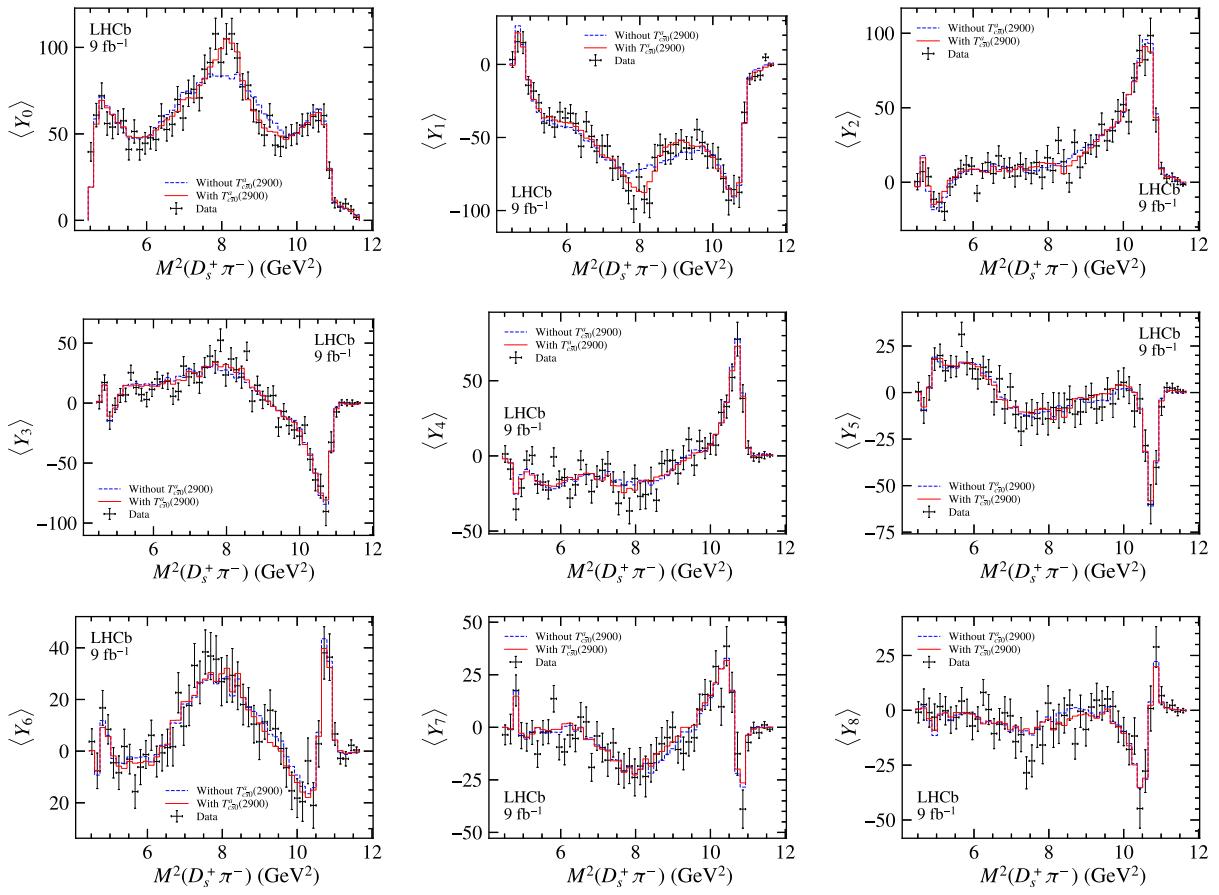
FIG. 18.   Moments analysis of $B^0 \to \overline{D}^0 D_s^+ \pi^-$ on $M^2(D_s^+ \pi^-)$. The black points indicate the data, while the blue and red histogram indicate the fit results without and with the $T_{c\bar{s}0}^a(2900)$ states separately.
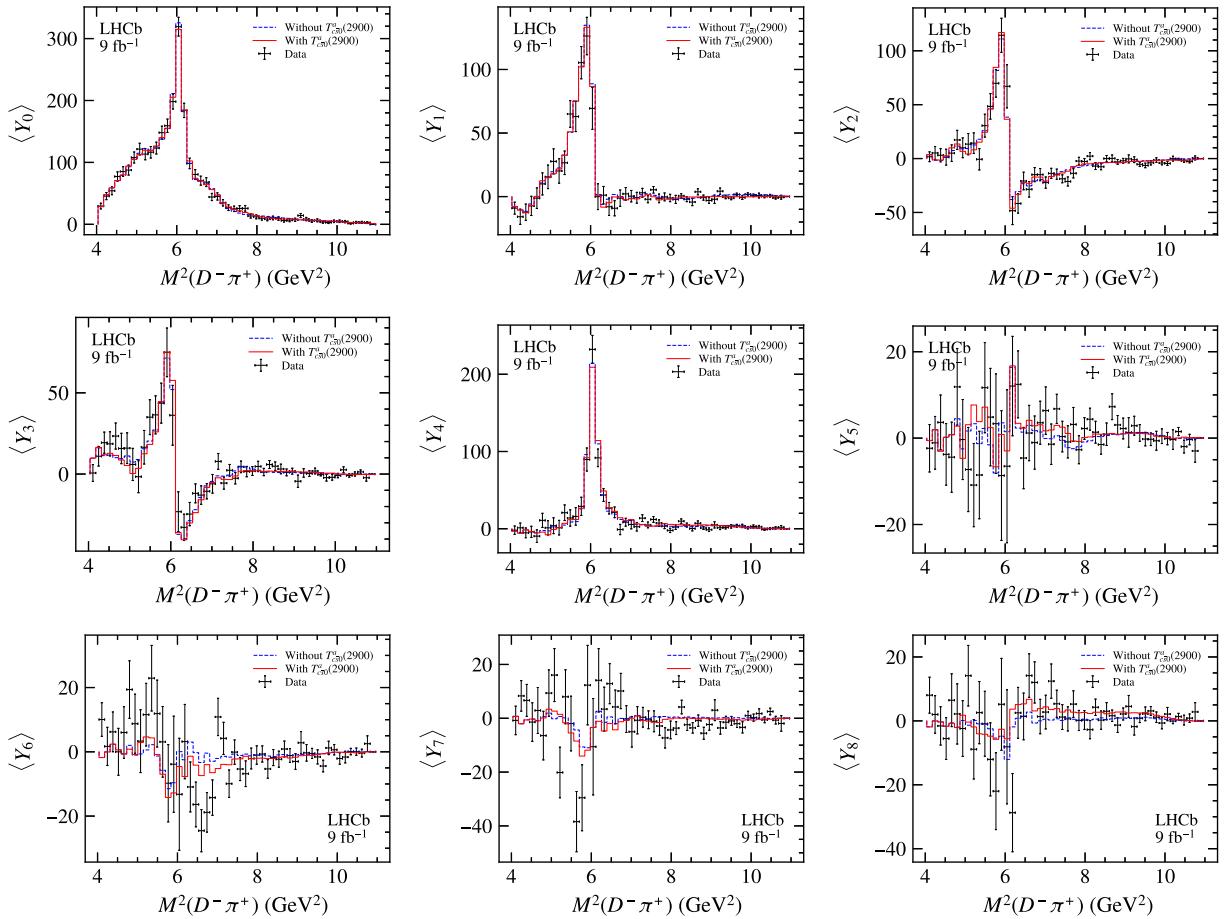
FIG. 19.   Moments analysis of $B^+ \rightarrow D^- D_s^+ \pi^+$ on $M^2(D^- \pi^+)$. The black points indicate the data, while the blue and red histogram indicate the fit results without and with the $T^a_{c\bar{s}0}(2900)$ states separately.
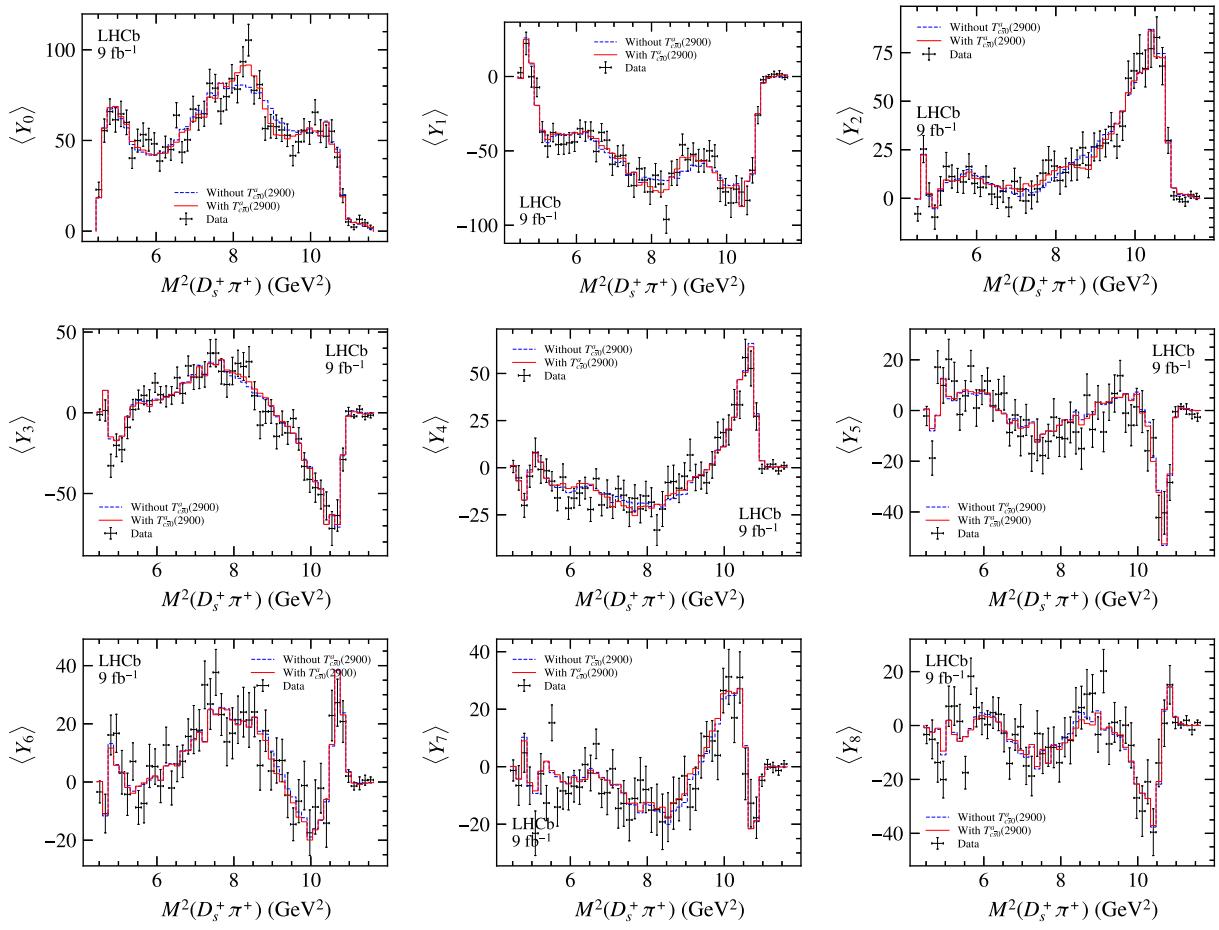
FIG. 20.   Moments analysis of $B^+ \to D^- D_s^+ \pi^+$ on $M^2(D_s^+ \pi^+)$. The black points indicate the data, while the blue and red histogram indicate the fit results without and with the $T_{c\bar{s}0}^a(2900)$ states separately.

[1] J. Brodzicka *et al.* (Belle Collaboration), Phys. Rev. Lett. **100,** 092001 (2008).

[2] J. P. Lees *et al.* (*BABAR* Collaboration), Phys. Rev. D **91,** 052002 (2015).

[3] R. Aaij *et al.* (LHCb Collaboration), Phys. Rev. Lett. **125,** 242001 (2020).

[4] R. Aaij *et al.* (LHCb Collaboration), Phys. Rev. D **102,** 112003 (2020).

[5] H.-X. Chen, Wei Chen, Xiang Liu, Yan-Rui Liu, and Shi-Lin Zhu, Rep. Prog. Phys. **86,** 026201 (2023).

[6] H.-X. Chen, Wei Chen, Xiang Liu, Yan-Rui Liu, and Shi-Lin Zhu, Rep. Prog. Phys. **80,** 076201 (2017).

[7] R. L. Workman (Particle Data Group), Prog. Theor. Exp. Phys. **2022,** 083C01 (2022).

[8] R. Aaij *et al.* (LHCb Collaboration), J. High Energy Phys. 09 (2013) 145.

[9] B. Aubert *et al.* (*BABAR* Collaboration), Phys. Rev. Lett. **90,** 242001 (2003).

[10] D. Besson *et al.* (CLEO Collaboration), Phys. Rev. D **68,** 032002 (2003).

[11] B. Aubert *et al.* (*BABAR* Collaboration), Phys. Rev. D **74,** 032007 (2006).

[12] S.-K. Choi *et al.* (Belle Collaboration), Phys. Rev. D **91,** 092011 (2015); **92,** 039905(A) (2015).

[13] V. M. Abazov *et al.* (D0 Collaboration), Phys. Rev. Lett. **117,** 022003 (2016).

[14] V. M. Abazov *et al.* (D0 Collaboration), Phys. Rev. D **97,** 092004 (2018).

[15] R. Aaij *et al.* (LHCb Collaboration), Phys. Rev. Lett. **117,** 152003 (2016).

[16] A. M. Sirunyan *et al.* (CMS Collaboration), Phys. Rev. Lett.**120,** 202005 (2018).

[17] M. Aaboud *et al.* (ATLAS Collaboration), Phys. Rev. Lett. **120,** 202007 (2018).

[18] T. Aaltonen *et al.* (CDF Collaboration), Phys. Rev. Lett. **120,** 202006 (2018).

[19] S. S. Agaev, K. Azizi, and H. Sundu, Phys. Rev. D **93,** 094006 (2016).

[20] W. Chen, Hua-Xing Chen, Xiang Liu, T. G. Steele, and Shi-Lin Zhu, Phys. Rev. D **95,** 114005 (2017).

[21] J. Baeza-Ballesteros, P. Hernández, and F. Romero-López, J. High Energy Phys. 06 (2022) 049.

[22] X.-G. He, W. Wang, and R. Zhu, Eur. Phys. J. C **80,** 1026 (2020).

[23] Q.-F. Lü, D.-Y. Chen, and Y.-B. Dong, Phys. Rev. D **102,** 074021 (2020).

[24] T. J. Burns and E. S. Swanson, Phys. Rev. D **103,** 014004 (2021).

[25] S. S. Agaev, K. Azizi, and H. Sundu, Nucl. Phys. **A1011,** 122202 (2021).

[26] S. S. Agaev, K. Azizi, and H. Sundu, Phys. Lett. B **820,** 136530 (2021).

[27] K. Azizi and U. Özdem, Phys. Rev. D **104,** 114002 (2021).

[28] M. Ablikim *et al.* (BESIII Collaboration), Phys. Rev. Lett. **126,** 102001 (2021).

[29] M. Ablikim *et al.* (BESIII Collaboration), Phys. Rev. Lett. **129,** 112003 (2022).

[30] R. Aaij *et al.* (LHCb Collaboration), Phys. Rev. Lett. **127,** 082001 (2021).

[31] R. Aaij *et al.* (LHCb Collaboration), companion Letter, Phys. Rev. Lett. **131,** 041902 (2023).

[32] A. A. Alves Jr. *et al.* (LHCb Collaboration), J. Instrum. **3,** S08005 (2008).

[33] R. Aaij *et al.* (LHCb Collaboration), Int. J. Mod. Phys. A **30,** 1530022 (2015).

[34] V. V. Gligorov and M. Williams, J. Instrum. **8,** P02013 (2013).

[35] T. Likhomanenko, P. Ilten, E. Khairullin, A. Rogozhnikov, A. Ustyuzhanin, and M. Williams, J. Phys. Conf. Ser. **664,** 082025 (2015).

[36] T. Sjöstrand, S. Mrenna, and P. Skands, Comput. Phys. Commun. **178,** 852 (2008).

[37] T. Sjöstrand, S. Mrenna, and P. Skands, J. High Energy Phys. 05 (2006) 026.

[38] I. Belyaev *et al.*, J. Phys. Conf. Ser. **331,** 032047 (2011).

[39] D. J. Lange, Nucl. Instrum. Methods Phys. Res., Sect. A **462,** 152 (2001).

[40] N. Davidson, T. Przedzinski, and Z. Was, Comput. Phys. Commun. **199,** 86 (2016).

[41] J. Allison *et al.* (Geant4 Collaboration), IEEE Trans. Nucl. Sci. **53,** 270 (2006).

[42] S. Agostinelli *et al.* (Geant4 Collaboration), Nucl. Instrum. Methods Phys. Res., Sect. A **506,** 250 (2003).

[43] M. Clemencic, G. Corti, S. Easo, C. R. Jones, S. Miglioranzi, M. Pappagallo, and P. Robbe, J. Phys. Conf. Ser. **331,** 032023 (2011).

[44] D. Müller, M. Clemencic, G. Corti, and M. Gersabeck, Eur. Phys. J. C **78,** 1009 (2018).

[45] A. Poluektov, J. Instrum. **10,** P02011 (2015).

[46] R. Aaij *et al.* (LHCb Collaboration), Phys. Rev. Lett. **110,** 182001 (2013).

[47] R. Aaij *et al.* (LHCb Collaboration), J. High Energy Phys. 06 (2013) 065.

[48] L. Breiman, J. H. Friedman, R. A. Olshen, and C. J. Stone, *Classification and Regression Trees* (Wadsworth International Group, Belmont, California, USA, 1984).

[49] Y. Freund and R. E. Schapire, J. Comput. Syst. Sci. **55,** 119 (1997).

[50] H. Voss, A. Hoecker, J. Stelzer, and F. Tegenfeldt, Proc. Sci. ACAT2007 (**2007**) 040.

[51] A. Hoecker *et al.*, arXiv:physics/0703039.

[52] W. D. Hulsbergen, Nucl. Instrum. Methods Phys. Res., Sect. A **552,** 566 (2005).

[53] T. Skwarnicki, A study of the radiative cascade transitions between the Upsilon-prime and Upsilon resonances, Ph.D. thesis, Institute of Nuclear Physics, XKrakow, 1986 [Report No. DESY-F31-86-02].

[54] G. N. Fleming, Phys. Rev. **135,** B551 (1964).

[55] D. Morgan, Phys. Rev. **166,** 1731 (1968).

[56] D. J. Herndon, P. Söding, and R. J. Cashmore, Phys. Rev. D **11,** 3165 (1975).

[57] F. Von Hippel and C. Quigg, Phys. Rev. D **5,** 624 (1972).

[58] R. Aaij *et al.* (LHCb Collaboration), Phys. Rev. D **94,** 072001 (2016).

[59] M.-L. Du, F.-K. Guo, C. Hanhart, B. Kubis, and U.-G. Meißner *et al.*, Phys. Rev. Lett. **126,** 192001 (2021).

[60] A. Mathad, D. O'Hanlon, A. Poluektov, and R. Rabadan, J. Instrum. **16,** P06016 (2021).

[61] T. Gershon (LHCb Collaboration), arXiv:2206.15233.

[62] R. Aaij *et al.* (LHCb Collaboration), Phys. Rev. D **92,** 032002 (2015).

[63] R. Aaij *et al.* (LHCb Collaboration), Phys. Rev. D **91,** 092002 (2015); **93,** 119901(E) (2016).

[64] R. Aaij *et al.* (LHCb Collaboration), Phys. Rev. D **92,** 012012 (2015).

[65] R. Aaij *et al.* (LHCb Collaboration), Phys. Rev. D **90,** 072003 (2014).

[66] H.-Y. Cheng and W.-S. Hou, Phys. Lett. B **566,** 193 (2003).

[67] T. E. Browder, S. Pakvasa, and A. A. Petrov, Phys. Lett. B **578,** 365 (2004).

[68] V. Dmitrasinovic, Phys. Rev. D **70,** 096011 (2004).

[69] V. Dmitrasinovic, Phys. Rev. D **86,** 016006 (2012).

[70] V. Dmitrasinovic, Phys. Rev. Lett. **94,** 162002 (2005).

[71] L. Maiani, F. Piccinini, A. D. Polosa, and V. Riquer, Phys. Rev. D **71,** 014028 (2005).

[72] L. Lyons, Ann. Appl. Stat. **2,** 887 (2008).

[73] B. Efron, Ann. Stat. **7,** 1 (1979).

R. Aaij[32], A. S. W. Abdelmotteleb[50], C. Abellan Beteta,[44] F. Abudinén[50], T. Ackernley[54], B. Adeva[40] M. Adinolfi[48], P. Adlarson[77], H. Afsharnia,[9] C. Agapopoulou[13], C. A. Aidala[78], S. Aiola[25], Z. Ajaltouni,[9] S. Akar[59], K. Akiba[32], J. Albrecht[15], F. Alessio[42], M. Alexander[53], A. Alfonso Albero[39], Z. Aliouche[56] P. Alvarez Cartelle[49], R. Amalric[13], S. Amato[2], J. L. Amey[48], Y. Amhis[11,42], L. An[42], L. Anderlini[22]

M. Andersson[44] A. Andreianov[38] M. Andreotti[21] D. Andreou[62] D. Ao[6] F. Archilli[17] A. Artamonov[38] M. Artuso[62] E. Aslanides[10] M. Atzeni[44] B. Audurier[12] S. Bachmann[17] M. Bachmayer[43] J. J. Back[50] A. Bailly-reyre,[13] P. Baladron Rodriguez[40] V. Balagura[12] W. Baldini[21] J. Baptista de Souza Leite[1] M. Barbetti[22,b] R. J. Barlow[56] S. Barsuk[11] W. Barter[55] M. Bartolini[49] F. Baryshnikov[38] J. M. Basels[14] G. Bassi[29,c] B. Batsukh[4] A. Battig[15] A. Bay[43] A. Beck[50] M. Becker[15] F. Bedeschi[29] I. B. Bediaga[1] A. Beiter,[62] V. Belavin[38] S. Belin[40] V. Bellee[44] K. Belous[38] I. Belov[38] I. Belyaev[38] G. Benane[10] G. Bencivenni[23] E. Ben-Haim[13] A. Berezhnoy[38] R. Bernet[44] S. Bernet Andres[76] D. Berninghoff,[17] H. C. Bernstein,[62] C. Bertella[56] A. Bertolin[28] C. Betancourt[44] F. Betti[42] Ia. Bezshyiko[44] S. Bhasin[48] J. Bhom[35] L. Bian[68] M. S. Bieker[15] N. V. Biesuz[21] S. Bifani[47] P. Billoir[13] A. Biolchini[32] M. Birch[55] F. C. R. Bishop[49] A. Bitadze[56] A. Bizzeti[] M. P. Blago[49] T. Blake[50] F. Blanc[43] J. E. Blank[15] S. Blusk[62] D. Bobulska[53] J. A. Boelhauve[15] O. Boente Garcia[12] T. Boettcher[59] A. Boldyrev[38] C. S. Bolognani[74] R. Bolzonella[21,d] N. Bondar[38,42] F. Borgato[28] S. Borghi[56] M. Borsato[17] J. T. Borsuk[35] S. A. Bouchiba[43] T. J. V. Bowcock[54] A. Boyer[42] C. Bozzi[21] M. J. Bradley,[55] S. Braun[60] A. Brea Rodriguez[40] J. Brodzicka[35] A. Brossa Gonzalo[40] J. Brown[54] D. Brundu[27] A. Buonaura[44] L. Buonincontri[28] A. T. Burke[56] C. Burr[42] A. Bursche,[66] A. Butkevich[38] J. S. Butter[32] J. Buytaert[42] W. Byczynski[42] S. Cadeddu[27] H. Cai,[68] R. Calabrese[21,d] L. Calefice[15] S. Cali[23] R. Calladine[47] M. Calvi[26,e] M. Calvo Gomez[76] P. Campana[23] D. H. Campora Perez[74] A. F. Campoverde Quezada[6] S. Capelli[26,e] L. Capriotti[20] A. Carbone[20,f] G. Carboni[31] R. Cardinale[24,g] A. Cardini[27] P. Carniti[26,e] L. Carus,[14] A. Casais Vidal[40] R. Caspary[17] G. Casse[54] M. Cattaneo[42] G. Cavallero[42] V. Cavallini[21,d] S. Celani[43] J. Cerasoli[10] D. Cervenkov[57] A. J. Chadwick[54] M. G. Chapman,[48] M. Charles[13] Ph. Charpentier[42] C. A. Chavez Barajas[54] M. Chefdeville[8] C. Chen[3] S. Chen[4] A. Chernov[35] S. Chernyshenko[46] V. Chobanova[40] S. Cholak[43] M. Chrzaszcz[35] A. Chubykin[38] V. Chulikov[38] P. Ciambrone[23] M. F. Cicala[50] X. Cid Vidal[40] G. Ciezarek[42] G. Ciullo[21,d] P. E. L. Clarke[52] M. Clemencic[42] H. V. Cliff[49] J. Closier[42] J. L. Cobbledick[56] V. Coco[42] J. A. B. Coelho[11] J. Cogan[10] E. Cogneras[9] L. Cojocariu[37] P. Collins[42] T. Colombo[42] L. Congedo[19] A. Contu[27] N. Cooke[47] I. Corredoira[40] G. Corti[42] B. Couturier[42] D. C. Craik[44] M. Cruz Torres[1,h] R. Currie[52] C. L. Da Silva[61] S. Dadabaev[38] L. Dai[65] X. Dai[5] E. Dall'Occo[15] J. Dalseno[40] C. D'Ambrosio[42] J. Daniel[9] A. Danilina[38] P. d'Argent[15] J. E. Davies[56] A. Davis[56] O. De Aguiar Francisco[56] J. de Boer[42] K. De Bruyn[73] S. De Capua[56] M. De Cian[43] U. De Freitas Carneiro Da Graca[1] E. De Lucia[23] J. M. De Miranda[1] L. De Paula[2] M. De Serio[19,i] D. De Simone[44] P. De Simone[23] F. De Vellis[15] J. A. de Vries[74] C. T. Dean[61] F. Debernardis[19,i] D. Decamp[8] V. Dedu[10] L. Del Buono[13] B. Delaney[58] H.-P. Dembinski[15] V. Denysenko[44] O. Deschamps[9] F. Dettori[27,j] B. Dey[71] A. Di Cicco[23] P. Di Nezza[23] I. Diachkov[38] S. Didenko[38] L. Dieste Maronas,[40] S. Ding[62] V. Dobishuk[46] A. Dolmatov,[38] C. Dong[3] A. M. Donohoe[18] F. Dordei[27] A. C. dos Reis[1] L. Douglas,[53] A. G. Downes[8] P. Duda[75] M. W. Dudek[35] L. Dufour[42] V. Duk[72] P. Durante[42] M. M. Duras[75] J. M. Durham[61] D. Dutta[56] A. Dziurda[35] A. Dzyuba[38] S. Easo[51] U. Egede[63] V. Egorychev[38] S. Eidelman,[38,a] C. Eirea Orro[40] S. Eisenhardt[52] E. Ejopu[56] S. Ek-In[43] L. Eklund[77] S. Ely[62] A. Ene[37] E. Epple[59] S. Escher[14] J. Eschle[44] S. Esen[44] T. Evans[56] F. Fabiano[27,j] L. N. Falcao[1] Y. Fan[6] B. Fang[68] L. Fantini[72,k] M. Faria[43] S. Farry[54] D. Fazzini[26,e] L. F Felkowski[75] M. Feo[42] M. Fernandez Gomez[40] A. D. Fernez[60] F. Ferrari[20] L. Ferreira Lopes[43] F. Ferreira Rodrigues[2] S. Ferreres Sole[32] M. Ferrillo[44] M. Ferro-Luzzi[42] S. Filippov[38] R. A. Fini[19] M. Fiorini[21,d] M. Firlej[34] K. M. Fischer[57] D. S. Fitzgerald[78] C. Fitzpatrick[56] T. Fiutowski[34] F. Fleuret[12] M. Fontana[13] F. Fontanelli[24,g] R. Forty[42] D. Foulds-Holt[49] V. Franco Lima[54] M. Franco Sevilla[60] M. Frank[42] E. Franzoso[21,d] G. Frau[17] C. Frei[42] D. A. Friday[53] J. Fu[6] Q. Fuehring[15] T. Fulghesu[13] E. Gabriel[32] G. Galati[19,i] M. D. Galati[32] A. Gallas Torreira[40] D. Galli[20,f] S. Gambetta[52,42] Y. Gan[3] M. Gandelman[2] P. Gandini[25] Y. Gao[7] Y. Gao[5] M. Garau[27,j] L. M. Garcia Martin[50] P. Garcia Moreno[39] J. García Pardiñas[26,e] B. Garcia Plana,[40] F. A. Garcia Rosales[12] L. Garrido[39] C. Gaspar[42] R. E. Geertsema[32] D. Gerick,[17] L. L. Gerken[15] E. Gersabeck[56] M. Gersabeck[56] T. Gershon[50] L. Giambastiani[28] V. Gibson[49] H. K. Giemza[36] A. L. Gilman[57] M. Giovannetti[23,l] A. Gioventù[40] P. Gironella Gironell[39] C. Giugliano[21,d] M. A. Giza[35] K. Gizdov[52] E. L. Gkougkousis[42] V. V. Gligorov[13,42] C. Göbel[64] E. Golobardes[76] D. Golubkov[38] A. Golutvin[55,38] A. Gomes[1,m] S. Gomez Fernandez[39] F. Goncalves Abrantes[57] M. Goncerz[35] G. Gong[3] I. V. Gorelov[38] C. Gotti[26]

J. P. Grabowski[70] T. Grammatico[13] L. A. Granado Cardoso[42] E. Graugés[39] E. Graverini[43] G. Graziani,
A. T. Grecu[37] L. M. Greeven[32] N. A. Grieser[4] L. Grillo[53] S. Gromov[38] B. R. Gruberg Cazon[57] C. Gu[3]
M. Guarise[21,d] M. Guittiere[11] P. A. Günther[17] E. Gushchin[38] A. Guth[14] Y. Guz[38] T. Gys[42] T. Hadavizadeh[63]
G. Haefeli[43] C. Haen[42] J. Haimberger[42] S. C. Haines[49] T. Halewood-leagas[54] M. M. Halvorsen[42]
P. M. Hamilton[60] J. Hammerich[54] Q. Han[7] X. Han[17] E. B. Hansen[56] S. Hansmann-Menzemer[17] L. Hao[6]
N. Harnew[57] T. Harrison[54] C. Hasse[42] M. Hatch[42] J. He[6,n] K. Heijhoff[32] C. Henderson[59]
R. D. L. Henderson[63,50] A. M. Hennequin[58] K. Hennessy[54] L. Henry[42] J. Herd[55] J. Heuel[14] A. Hicheur[2]
D. Hill[43] M. Hilton[56] S. E. Hollitt[15] J. Horswill[56] R. Hou[7] Y. Hou[8] J. Hu[17] J. Hu[66] W. Hu[5] X. Hu[3]
W. Huang[6] X. Huang[68] W. Hulsbergen[32] R. J. Hunter[50] M. Hushchyn[38] D. Hutchcroft[54] P. Ibis[15] M. Idzik[34]
D. Ilin[38] P. Ilten[59] A. Inglessi[38] A. Iniukhin[38] A. Ishteev[38] K. Ivshin[38] R. Jacobsson[42] H. Jage[14]
S. J. Jaimes Elles[41] S. Jakobsen[42] E. Jans[32] B. K. Jashal[41] A. Jawahery[60] V. Jevtic[15] E. Jiang[60] X. Jiang[4,6]
Y. Jiang[6] M. John[57] D. Johnson[58] C. R. Jones[49] T. P. Jones[50] B. Jost[42] N. Jurik[42] I. Juszczak[35]
S. Kandybei[45] Y. Kang[3] M. Karacson[42] D. Karpenkov[38] M. Karpov[38] J. W. Kautz[59] F. Keizer[42]
D. M. Keller[62] M. Kenzie[50] T. Ketel[32] B. Khanji[15] A. Kharisova[38] S. Kholodenko[38] G. Khreich[11]
T. Kirn[14] V. S. Kirsebom[43] O. Kitouni[58] S. Klaver[33] N. Kleijne[29,c] K. Klimaszewski[36] M. R. Kmiec[36]
S. Koliiev[46] A. Kondybayeva[38] A. Konoplyannikov[38] P. Kopciewicz[34] R. Kopecna,[17] P. Koppenburg[32]
M. Korolev[38] I. Kostiuk[32,46] O. Kot,[46] S. Kotriakhova[32] A. Kozachuk[38] P. Kravchenko[38] L. Kravchuk[38]
R. D. Krawczyk[42] M. Kreps[50] S. Kretzschmar[14] P. Krokovny[38] W. Krupa[34] W. Krzemien[36] J. Kubat,[17]
S. Kubis[75] W. Kucewicz[35,34] M. Kucharczyk[35] V. Kudryavtsev[38] A. Kupsc[77] D. Lacarrere[42] G. Lafferty[56]
A. Lai,[27] A. Lampis[27,j] D. Lancierini[44] C. Landesa Gomez[40] J. J. Lane[56] R. Lane,[48] G. Lanfranchi[23]
C. Langenbruch[14] J. Langer[15] O. Lantwin[38] T. Latham[50] F. Lazzari[29,o] M. Lazzaroni[25,p] R. Le Gac[10]
S. H. Lee[78] R. Lefèvre[9] A. Leflat[38] S. Legotin[38] P. Lenisa[21,d] O. Leroy[10] T. Lesiak[35] B. Leverington[17]
A. Li,[3] H. Li[66] K. Li[7] P. Li[17] P.-R. Li[67] S. Li[7] T. Li[4] T. Li[66] Y. Li[4] Z. Li[62] X. Liang[62] C. Lin[6]
T. Lin[51] R. Lindner[42] V. Lisovskyi[15] R. Litvinov[27,j] G. Liu[66] H. Liu[6] Q. Liu[6] S. Liu[4,6] Y. Liu[6]
A. Lobo Salvia[39] A. Loi[27] R. Lollini[72] J. Lomba Castro[40] I. Longstaff[53] J. H. Lopes[2] A. Lopez Huertas[39]
S. López Soliño[40] G. H. Lovell[49] Y. Lu[4,q] C. Lucarelli[22,b] D. Lucchesi[28,r] S. Luchuk[38] M. Lucio Martinez[74]
V. Lukashenko[32,46] Y. Luo[3] A. Lupato[56] E. Luppi[21,d] A. Lusiani[29,c] K. Lynch[18] X.-R. Lyu[6] L. Ma[4]
R. Ma,[6] S. Maccolini[20] F. Machefert[11] F. Maciuc[37] I. Mackay[57] V. Macko[43] P. Mackowiak[15]
L. R. Madhan Mohan[48] A. Maevskiy[38] D. Maisuzenko[38] M. W. Majewski[34] J. J. Malczewski[35] S. Malde[57]
B. Malecki[35,42] A. Malinin[38] T. Maltsev[38] G. Manca[27,j] G. Mancinelli[10] C. Mancuso[11,25,p] D. Manuzzi[20]
C. A. Manzari[44] D. Marangotto[25,p] J. F. Marchand[8] U. Marconi[20] S. Mariani[22,b] C. Marin Benito[39]
J. Marks[17] A. M. Marshall[48] P. J. Marshall,[54] G. Martelli[72,k] G. Martellotti[30] L. Martinazzoli[42,e]
M. Martinelli[26,e] D. Martinez Santos[40] F. Martinez Vidal[41] A. Massafferri[1] M. Materok[14] R. Matev[42]
A. Mathad[44] V. Matiunin[38] C. Matteuzzi[26] K. R. Mattioli[12] A. Mauri[32] E. Maurice[12] J. Mauricio[39]
M. Mazurek[42] M. McCann[55] L. Mcconnell,[18] T. H. McGrath[56] N. T. McHugh[53] A. McNab[56] R. McNulty[18]
J. V. Mead[54] B. Meadows[59] G. Meier[15] D. Melnychuk[36] S. Meloni[26,e] M. Merk[32,74] A. Merli[25,p]
L. Meyer Garcia[2] D. Miao[4,6] M. Mikhasenko[70,s] D. A. Milanes[69] E. Millard,[50] M. Milovanovic[42]
M.-N. Minard,[8,a] A. Minotti[26,e] T. Miralles[9] S. E. Mitchell[52] B. Mitreska[56] D. S. Mitzel[15] A. Mödden[15]
R. A. Mohammed[57] R. D. Moise[14] S. Mokhnenko[38] T. Mombächer[40] M. Monk[50,63] I. A. Monroy[69]
S. Monteil[9] M. Morandin[28] G. Morello[23] M. J. Morello[29,c] J. Moron[34] A. B. Morris[70] A. G. Morris[50]
R. Mountain[62] H. Mu[3] E. Muhammad[50] F. Muheim[52] M. Mulder[73] K. Müller[44] C. H. Murphy[57]
D. Murray[56] R. Murta[55] P. Muzzetto[27,j] P. Naik[48] T. Nakada[43] R. Nandakumar[51] T. Nanut[42] I. Nasteva[2]
M. Needham[52] N. Neri[25,p] S. Neubert[70] N. Neufeld[42] P. Neustroev,[38] R. Newcombe[55] J. Nicolini[15,11]
E. M. Niel[43] S. Nieswand,[14] N. Nikitin[38] N. S. Nolte[58] C. Normand[8,27,j] J. Novoa Fernandez[40] C. Nunez[78]
A. Oblakowska-Mucha[34] V. Obraztsov[38] T. Oeser[14] D. P. O'Hanlon[48] S. Okamura[21,d] R. Oldeman[27,j]
F. Oliva[52] C. J. G. Onderwater[73] R. H. O'Neil[52] J. M. Otalora Goicochea[2] T. Ovsiannikova[38] P. Owen[44]
A. Oyanguren[41] O. Ozcelik[52] K. O. Padeken[70] B. Pagare[50] P. R. Pais[42] T. Pajero[57] A. Palano[19]
M. Palutan[23] Y. Pan[56] G. Panshin[38] L. Paolucci[50] A. Papanestis[51] M. Pappagallo[19,i] L. L. Pappalardo[21,d]
C. Pappenheimer[59] W. Parker[60] C. Parkes[56] B. Passalacqua[21,d] G. Passaleva[22] A. Pastore[19] M. Patel[55]

C. Patrignani[20,f] C. J. Pawley[74] A. Pearce[42] A. Pellegrino[32] M. Pepe Altarelli[42] S. Perazzini[20] D. Pereima[38] A. Pereiro Castro[40] P. Perret[9] M. Petric[53] K. Petridis[48] A. Petrolini[24,g] A. Petrov[38] S. Petrucci[52] M. Petruzzo[25] H. Pham[62] A. Philippov[38] R. Piandani[6] L. Pica[29,c] M. Piccini[72] B. Pietrzyk[8] G. Pietrzyk[11] M. Pili[57] D. Pinci[30] F. Pisani[42] M. Pizzichemi[26,42,e] V. Placinta[37] J. Plews[47] M. Plo Casasus[40] F. Polci[13,42] M. Poli Lener[23] M. Poliakova[62] A. Poluektov[10] N. Polukhina[38] I. Polyakov[42] E. Polycarpo[2] S. Ponce[42] D. Popov[6,42] S. Popov[38] S. Poslavskii[38] K. Prasanth[35] L. Promberger[17] C. Prouve[40] V. Pugatch[46] V. Puill[11] G. Punzi[29,t] H. R. Qi[3] W. Qian[6] N. Qin[3] S. Qu[3] R. Quagliani[43] N. V. Raab[18] R. I. Rabadan Trejo[6] B. Rachwal[34] J. H. Rademacker[48] R. Rajagopalan[62] M. Rama[29] M. Ramos Pernas[50] M. S. Rangel[2] F. Ratnikov[38] G. Raven[33,42] M. Rebollo De Miguel[41] F. Redi[42] J. Reich[48] F. Reiss[56] C. Remon Alepuz,[41] Z. Ren[3] P. K. Resmi[10] R. Ribatti[29,c] A. M. Ricci[27] S. Ricciardi[51] K. Richardson[58] M. Richardson-Slipper[52] K. Rinnert[54] P. Robbe[11] G. Robertson[52] A. B. Rodrigues[43] E. Rodrigues[54] E. Rodriguez Fernandez[40] J. A. Rodriguez Lopez[69] E. Rodriguez Rodriguez[40] D. L. Rolf[42] A. Rollings[57] P. Roloff[42] V. Romanovskiy[38] M. Romero Lamas[40] A. Romero Vidal[40] J. D. Roth,[78,a] M. Rotondo[23] M. S. Rudolph[62] T. Ruf[42] R. A. Ruiz Fernandez[40] J. Ruiz Vidal,[41] A. Ryzhikov[38] J. Ryzka[34] J. J. Saborido Silva[40] N. Sagidova[38] N. Sahoo[47] B. Saitta[27,j] M. Salomoni[42] C. Sanchez Gras[32] I. Sanderswood[41] R. Santacesaria[30] C. Santamarina Rios[40] M. Santimaria[23] E. Santovetti[31,l] D. Saranin[38] G. Sarpis[14] M. Sarpis[70] A. Sarti[30] C. Satriano[30,u] A. Satta[31] M. Saur[15] D. Savrina[38] H. Sazak[9] L. G. Scantlebury Smead[57] A. Scarabotto[13] S. Schael[14] S. Scherl[54] M. Schiller[53] H. Schindler[42] M. Schmelling[16] B. Schmidt[42] S. Schmitt[14] O. Schneider[43] A. Schopper[42] M. Schubiger[32] S. Schulte[43] M. H. Schune[11] R. Schwemmer[42] B. Sciascia[23,42] A. Sciuccati[42] S. Sellam[40] A. Semennikov[38] M. Senghi Soares[33] A. Sergi[24,g] N. Serra[44] L. Sestini[28] A. Seuthe[15] Y. Shang[5] D. M. Shangase[78] M. Shapkin[38] I. Shchemerov[38] L. Shchutska[43] T. Shears[54] L. Shekhtman[38] Z. Shen[5] S. Sheng[4,6] V. Shevchenko[38] B. Shi[6] E. B. Shields[26,e] Y. Shimizu[11] E. Shmanin[38] R. Shorkin[38] J. D. Shupperd[62] B. G. Siddi[21,d] R. Silva Coutinho[62] G. Simi[28] S. Simone[19,i] M. Singla[63] N. Skidmore[56] R. Skuza[17] T. Skwarnicki[62] M. W. Slater[47] J. C. Smallwood[57] J. G. Smeaton[49] E. Smith[44] K. Smith[61] M. Smith[55] A. Snoch[32] L. Soares Lavra[9] M. D. Sokoloff[59] F. J. P. Soler[53] A. Solomin[38,48] A. Solovev[38] I. Solovyev[38] R. Song[63] F. L. Souza De Almeida[2] B. Souza De Paula[2] B. Spaan,[15,a] E. Spadaro Norella[25,p] E. Spedicato[20] E. Spiridenkov,[38] P. Spradlin[53] V. Sriskaran[42] F. Stagni[42] M. Stahl[42] S. Stahl[42] S. Stanislaus[57] E. N. Stein[42] O. Steinkamp[44] O. Stenyakin,[38] H. Stevens[15] S. Stone,[62,a] D. Strekalina[38] F. Suljik[57] J. Sun[27] L. Sun[68] Y. Sun[60] P. Svihra[56] P. N. Swallow[47] K. Swientek[34] A. Szabelski[36] T. Szumlak[34] M. Szymanski[42] Y. Tan[3] S. Taneja[56] A. R. Tanner,[48] M. D. Tat[57] A. Terentev[38] F. Teubert[42] E. Thomas[42] D. J. D. Thompson[47] K. A. Thomson[54] H. Tilquin[55] V. Tisserand[9] S. T'Jampens[8] M. Tobin[4] L. Tomassetti[21,d] G. Tonani[25,p] X. Tong[5] D. Torres Machado[1] D. Y. Tou[3] S. M. Trilov,[48] C. Trippl[43] G. Tuci[6] A. Tully[43] N. Tuning[32] A. Ukleja[36] D. J. Unverzagt[17] A. Usachov[32] A. Ustyuzhanin[38] U. Uwer[17] A. Vagner,[38] V. Vagnoni[20] A. Valassi[42] G. Valenti[20] N. Valls Canudas[76] M. van Beuzekom[32] M. Van Dijk[43] H. Van Hecke[61] E. van Herwijnen[55] C. B. Van Hulse[40,v] M. van Veghel[73] R. Vazquez Gomez[39] P. Vazquez Regueiro[40] C. Vázquez Sierra[42] S. Vecchi[21] J. J. Velthuis[48] M. Veltri[22,w] A. Venkateswaran[43] M. Veronesi[32] M. Vesterinen[50] D. Vieira[59] M. Vieites Diaz[43] X. Vilasis-Cardona[76] E. Vilella Figueras[54] A. Villa[20] P. Vincent[13] F. C. Volle[11] D. vom Bruch[10] A. Vorobyev,[38] V. Vorobyev,[38] N. Voropaev[38] K. Vos[74] C. Vrahas[52] R. Waldi[17] J. Walsh[29] G. Wan[5] C. Wang[17] G. Wang[7] J. Wang[5] J. Wang[4] J. Wang[3] J. Wang[68] M. Wang[5] R. Wang[48] X. Wang[66] Y. Wang[7] Z. Wang[44] Z. Wang[3] Z. Wang[6] J. A. Ward[50,63] N. K. Watson[47] D. Websdale[55] Y. Wei[5] C. Weisser,[58] B. D. C. Westhenry[48] D. J. White[56] M. Whitehead[53] A. R. Wiederhold[50] D. Wiedner[15] G. Wilkinson[57] M. K. Wilkinson[59] I. Williams,[49] M. Williams[58] M. R. J. Williams[52] R. Williams[49] F. F. Wilson[51] W. Wislicki[36] M. Witek[35] L. Witola[17] C. P. Wong[61] G. Wormser[11] S. A. Wotton[49] H. Wu[62] J. Wu[7] K. Wyllie[42] Z. Xiang[6] D. Xiao[7] Y. Xie[7] A. Xu[5] J. Xu[6] L. Xu[3] L. Xu[3] M. Xu[50] Q. Xu,[6] Z. Xu[9] Z. Xu[6] D. Yang[3] S. Yang[6] X. Yang[5] Y. Yang[6] Z. Yang[5] Z. Yang[60] L. E. Yeomans[54] V. Yeroshenko[11] H. Yeung[56] H. Yin[7] J. Yu[65] X. Yuan[62] E. Zaffaroni[43]

M. Zavertyaev[16] M. Zdybal[35] O. Zenaiev[42] M. Zeng[3] C. Zhang[5] D. Zhang[7] L. Zhang[3] S. Zhang[65] S. Zhang[5] Y. Zhang[5] Y. Zhang,[57] A. Zharkova[38] A. Zhelezov[17] Y. Zheng[6] T. Zhou[5] X. Zhou[6] Y. Zhou[6] V. Zhovkovska[11] X. Zhu[3] X. Zhu[7] Z. Zhu[6] V. Zhukov[14,38] Q. Zou[4,6] S. Zucchelli[20,f] D. Zuliani[28] and G. Zunica[56]

(LHCb Collaboration)

[1]*Centro Brasileiro de Pesquisas Físicas (CBPF), Rio de Janeiro, Brazil*
[2]*Universidade Federal do Rio de Janeiro (UFRJ), Rio de Janeiro, Brazil*
[3]*Center for High Energy Physics, Tsinghua University, Beijing, China*
[4]*Institute Of High Energy Physics (IHEP), Beijing, China*
[5]*School of Physics State Key Laboratory of Nuclear Physics and Technology,
Peking University, Beijing, China*
[6]*University of Chinese Academy of Sciences, Beijing, China*
[7]*Institute of Particle Physics, Central China Normal University, Wuhan, Hubei, China*
[8]*Université Savoie Mont Blanc, CNRS, IN2P3-LAPP, Annecy, France*
[9]*Université Clermont Auvergne, CNRS/IN2P3, LPC, Clermont-Ferrand, France*
[10]*Aix Marseille Univ, CNRS/IN2P3, CPPM, Marseille, France*
[11]*Université Paris-Saclay, CNRS/IN2P3, IJCLab, Orsay, France*
[12]*Laboratoire Leprince-Ringuet, CNRS/IN2P3, Ecole Polytechnique,
Institut Polytechnique de Paris, Palaiseau, France*
[13]*LPNHE, Sorbonne Université, Paris Diderot Sorbonne Paris Cité, CNRS/IN2P3, Paris, France*
[14]*I. Physikalisches Institut, RWTH Aachen University, Aachen, Germany*
[15]*Fakultät Physik, Technische Universität Dortmund, Dortmund, Germany*
[16]*Max-Planck-Institut für Kernphysik (MPIK), Heidelberg, Germany*
[17]*Physikalisches Institut, Ruprecht-Karls-Universität Heidelberg, Heidelberg, Germany*
[18]*School of Physics, University College Dublin, Dublin, Ireland*
[19]*INFN Sezione di Bari, Bari, Italy*
[20]*INFN Sezione di Bologna, Bologna, Italy*
[21]*INFN Sezione di Ferrara, Ferrara, Italy*
[22]*INFN Sezione di Firenze, Firenze, Italy*
[23]*INFN Laboratori Nazionali di Frascati, Frascati, Italy*
[24]*INFN Sezione di Genova, Genova, Italy*
[25]*INFN Sezione di Milano, Milano, Italy*
[26]*INFN Sezione di Milano-Bicocca, Milano, Italy*
[27]*INFN Sezione di Cagliari, Monserrato, Italy*
[28]*Università degli Studi di Padova, Università e INFN, Padova, Padova, Italy*
[29]*INFN Sezione di Pisa, Pisa, Italy*
[30]*INFN Sezione di Roma La Sapienza, Roma, Italy*
[31]*INFN Sezione di Roma Tor Vergata, Roma, Italy*
[32]*Nikhef National Institute for Subatomic Physics, Amsterdam, Netherlands*
[33]*Nikhef National Institute for Subatomic Physics and VU University Amsterdam, Amsterdam, Netherlands*
[34]*AGH—University of Science and Technology,
Faculty of Physics and Applied Computer Science, Kraków, Poland*
[35]*Henryk Niewodniczanski Institute of Nuclear Physics Polish Academy of Sciences, Kraków, Poland*
[36]*National Center for Nuclear Research (NCBJ), Warsaw, Poland*
[37]*Horia Hulubei National Institute of Physics and Nuclear Engineering, Bucharest-Magurele, Romania*
[38]*Affiliated with an institute covered by a cooperation agreement with CERN*
[39]*ICCUB, Universitat de Barcelona, Barcelona, Spain*
[40]*Instituto Galego de Física de Altas Enerxías (IGFAE), Universidade de Santiago de Compostela,
Santiago de Compostela, Spain*
[41]*Instituto de Fisica Corpuscular, Centro Mixto Universidad de Valencia—CSIC, Valencia, Spain*
[42]*European Organization for Nuclear Research (CERN), Geneva, Switzerland*
[43]*Institute of Physics, Ecole Polytechnique Fédérale de Lausanne (EPFL), Lausanne, Switzerland*
[44]*Physik-Institut, Universität Zürich, Zürich, Switzerland*
[45]*NSC Kharkiv Institute of Physics and Technology (NSC KIPT), Kharkiv, Ukraine*
[46]*Institute for Nuclear Research of the National Academy of Sciences (KINR), Kyiv, Ukraine*
[47]*University of Birmingham, Birmingham, United Kingdom*
[48]*H.H. Wills Physics Laboratory, University of Bristol, Bristol, United Kingdom*

[49]Cavendish Laboratory, University of Cambridge, Cambridge, United Kingdom

[50]Department of Physics, University of Warwick, Coventry, United Kingdom

[51]STFC Rutherford Appleton Laboratory, Didcot, United Kingdom

[52]School of Physics and Astronomy, University of Edinburgh, Edinburgh, United Kingdom

[53]School of Physics and Astronomy, University of Glasgow, Glasgow, United Kingdom

[54]Oliver Lodge Laboratory, University of Liverpool, Liverpool, United Kingdom

[55]Imperial College London, London, United Kingdom

[56]Department of Physics and Astronomy, University of Manchester, Manchester, United Kingdom

[57]Department of Physics, University of Oxford, Oxford, United Kingdom

[58]Massachusetts Institute of Technology, Cambridge, Massachusetts, United States

[59]University of Cincinnati, Cincinnati, Ohio, United States

[60]University of Maryland, College Park, Maryland, United States

[61]Los Alamos National Laboratory (LANL), Los Alamos, New Mexico, United States

[62]Syracuse University, Syracuse, New York, United States

[63]School of Physics and Astronomy, Monash University, Melbourne, Australia (associated with Department of Physics, University of Warwick, Coventry, United Kingdom)

[64]Pontifícia Universidade Católica do Rio de Janeiro (PUC-Rio), Rio de Janeiro, Brazil (associated with Universidade Federal do Rio de Janeiro (UFRJ), Rio de Janeiro, Brazil)

[65]Physics and Micro Electronic College, Hunan University, Changsha City, China (associated with Institute of Particle Physics, Central China Normal University, Wuhan, Hubei, China)

[66]Guangdong Provincial Key Laboratory of Nuclear Science, Guangdong-Hong Kong Joint Laboratory of Quantum Matter, Institute of Quantum Matter, South China Normal University, Guangzhou, China (associated with Center for High Energy Physics, Tsinghua University, Beijing, China)

[67]Lanzhou University, Lanzhou, China (associated with Institute Of High Energy Physics (IHEP), Beijing, China)

[68]School of Physics and Technology, Wuhan University, Wuhan, China (associated with Center for High Energy Physics, Tsinghua University, Beijing, China)

[69]Departamento de Fisica, Universidad Nacional de Colombia, Bogota, Colombia (associated with LPNHE, Sorbonne Université, Paris Diderot Sorbonne Paris Cité, CNRS/IN2P3, Paris, France)

[70]Universität Bonn—Helmholtz-Institut für Strahlen und Kernphysik, Bonn, Germany (associated with Physikalisches Institut, Ruprecht-Karls-Universität Heidelberg, Heidelberg, Germany)

[71]Eotvos Lorand University, Budapest, Hungary (associated with European Organization for Nuclear Research (CERN), Geneva, Switzerland)

[72]INFN Sezione di Perugia, Perugia, Italy (associated with INFN Sezione di Ferrara, Ferrara, Italy)

[73]Van Swinderen Institute, University of Groningen, Groningen, Netherlands (associated with Nikhef National Institute for Subatomic Physics, Amsterdam, Netherlands)

[74]Universiteit Maastricht, Maastricht, Netherlands (associated with Nikhef National Institute for Subatomic Physics, Amsterdam, Netherlands)

[75]Tadeusz Kosciuszko Cracow University of Technology, Cracow, Poland (associated with Henryk Niewodniczanski Institute of Nuclear Physics Polish Academy of Sciences, Kraków, Poland)

[76]DS4DS, La Salle, Universitat Ramon Llull, Barcelona, Spain (associated with ICCUB, Universitat de Barcelona, Barcelona, Spain)

[77]Department of Physics and Astronomy, Uppsala University, Uppsala, Sweden (associated with School of Physics and Astronomy, University of Glasgow, Glasgow, United Kingdom)

[78]University of Michigan, Ann Arbor, Michigan, United States (associated with Syracuse University, Syracuse, New York, United States)

[a]Deceased.

[b]Also at Università di Firenze, Firenze, Italy.

[c]Also at Scuola Normale Superiore, Pisa, Italy.

[d]Also at Università di Ferrara, Ferrara, Italy.

[e]Also at Università di Milano Bicocca, Milano, Italy.

[f]Also at Università di Bologna, Bologna, Italy.

[g]Also at Università di Genova, Genova, Italy.

[h]Also at Universidad Nacional Autónoma de Honduras, Tegucigalpa, Honduras.

[i]Also at Università di Bari, Bari, Italy.

[j]Also at Università di Cagliari, Cagliari, Italy.

[k]Also at Università di Perugia, Perugia, Italy.

[l]Also at Università di Roma Tor Vergata, Roma, Italy.

[m]Also at Universidade de Brasília, Brasília, Brazil.

[n]Also at Hangzhou Institute for Advanced Study, UCAS, Hangzhou, China.

[o]Also at Università di Siena, Siena, Italy.

[p]Also at Università degli Studi di Milano, Milano, Italy.

[q]Also at Central South U., Changsha, China.

[r]Also at Università di Padova, Padova, Italy.

[s]Also at Excellence Cluster ORIGINS, Munich, Germany.

[t]Also at Università di Pisa, Pisa, Italy.

[u]Also at Università della Basilicata, Potenza, Italy.

[v]Also at Universidad de Alcalá, Alcalá de Henares, Spain.

[w]Also at Università di Urbino, Urbino, Italy.